

THE VIEWS AND CONCLUSIONS CONTAINED IN THIS DOCUMENT ARE THOSE OF THE AUTHORS AND SHOULD NOT BE INTERPRETED AS NECESSARILY REPRESENTING THE OFFICIAL POLICIES, EITHER EXPRESS OR IMPLIED, OF THE DEFENSE ADVANCED RESEARCH PROJECTS AGENCY OR THE U. S. GOVERNMENT.

12

ONE METER KrF LASER SYSTEM

LEVEL III

A051534

J. A. Mangano, J. C. Hsia
Avco Everett Research Laboratory, Inc.
2385 Revere Beach Parkway
Everett, MA 02149

DDC
PREPARED
MAY 29 1979
C

Semi-Annual Report for Period 24 November 1977 - 24 May 1978

APPROVED FOR PUBLIC RELEASE; DISTRIBUTION UNLIMITED.

AD A069053

DDC FILE COPY

Sponsored by
DEFENSE ADVANCED RESEARCH PROJECTS AGENCY
DARPA Order No. 3125

Monitored by
OFFICE OF NAVAL RESEARCH
DEPARTMENT OF THE NAVY
Arlington, VA 22217

79 05 25 052

FOREWORD

DARPA Order No: 3125

Contractor: Avco Everett Research Laboratory, Inc.

Effective Date of Contract: August 23, 1976

Contract Expiration Date: February 28, 1979

Contract No: N00014-76-C-1032

Short Title of Work: One-Meter KrF Laser System

Principal Investigator and Phone No. J.A. Mangano
(617) 389-3000, Ext. 725

Scientific Officer: Director Physics Program, Physical
Science Division

Office of Naval Research
800 North Quincy Street
Arlington, VA 22217

Amount of Contract: \$1,678,470

UNCLASSIFIED

SECURITY CLASSIFICATION OF THIS PAGE (When Data Entered)

| REPORT DOCUMENTATION PAGE | | READ INSTRUCTIONS BEFORE COMPLETING FORM |
|--|-----------------------|---|
| 1. REPORT NUMBER | 2. GOVT ACCESSION NO. | 3. RECIPIENT'S CATALOG NUMBER |
| 4. TITLE (and Subtitle) ONE METER KrF LASER SYSTEM | | 5. TYPE OF REPORT & PERIOD COVERED Semi-Annual <i>rept.</i> 24 Nov 1977-24 May 1978 |
| 6. AUTHOR(s) J.A. Mangano, J.C. Hsia, J.H. Jacob, M. Rokni, C. Duzy | | 7. PERFORMING ORG. REPORT NUMBER |
| 8. CONTRACT OR GRANT NUMBER(s) N00014-76-C-10325 | | 9. PROGRAM ELEMENT, PROJECT, TASK AREA & WORK UNIT NUMBERS DARPA Order-3125 |
| 9. PERFORMING ORGANIZATION NAME AND ADDRESS Avco Everett Research Laboratory, Inc. 2385 Revere Beach Parkway Everett, MA 02149 | | 10. SECURITY CLASS. (of this report) Unclassified |
| 11. CONTROLLING OFFICE NAME AND ADDRESS Defense Advanced Research Projects Agency DARPA Order No. 3125 | | 11. DECLASSIFICATION/DOWNGRADING SCHEDULE |
| 12. MONITORING AGENCY NAME & ADDRESS (if different from Controlling Office) Office of Naval Research Department of the Navy Arlington, VA 22217 | | 12. REPORT DATE |
| 13. DISTRIBUTION STATEMENT (of this Report) Approved for public release; distribution unlimited <i>11 24 May 78</i> | | 13. NUMBER OF PAGES 79 |
| 14. DISTRIBUTION STATEMENT (of the abstract entered in Block 20, if different from Report) <i>12 84p.</i> | | 14. SECURITY CLASS. (of this report) Unclassified |
| 15. SUPPLEMENTARY NOTES | | |
| 16. KEY WORDS (Continue on reverse side if necessary and identify by block number) Rare Gas-Halide Lasers Laser Kinetics High Power UV Lasers KrF Lasers 79 05 25 052 XeF Lasers Laser Modeling | | |
| 17. ABSTRACT (Continue on reverse side if necessary and identify by block number) This interim technical report covers DARPA-sponsored research directed towards high power rare gas-halide lasers. The key issues being addressed are: 1) kinetics leading to laser medium gain and absorption, 2) laser energy extraction, 3) upper and lower laser state kinetics, 4) intrinsic laser efficiency, specific energy, and 5) energy scaling. By operating at elevated temperatures and e-beam pumped XeF laser intrinsic efficiency of 5.5% was obtained. | | |

048450

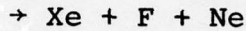
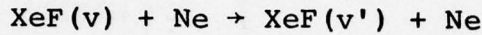
next page JB

UNCLASSIFIED

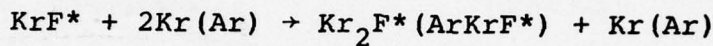
SECURITY CLASSIFICATION OF THIS PAGE(When Data Entered)

(20)

at a specific pulse energy of 5 J/l. The increase in efficiency is attributed to improved energy extraction from the XeF*(B) vibrational manifold and to decreased lifetime of the XeF ground state. Detailed comparisons were made between KrF laser experiments and model calculations. Excellent agreement was obtained. The comparison also suggests the importance of KrF* vibrational-rotational relaxation and B and C state mixing on laser performance at pump intensities exceeding (10^6 W/cm^2) . The rate constants for the reactions



and



have been calculated theoretically.

1,000,000 $\frac{\text{W}}{\text{cm}^2}$

| | |
|---------------------------------|---|
| ACCESSION for | |
| NTIS | Write Section <input checked="" type="checkbox"/> |
| DDC | B ff Section <input type="checkbox"/> |
| UNANNOUNCED | <input type="checkbox"/> |
| JUSTIFICATION | |
| BY | |
| DISTRIBUTION/AVAILABILITY CODES | |
| Dist: | SPECIAL |
| A | |

UNCLASSIFIED

SECURITY CLASSIFICATION OF THIS PAGE(When Data Entered)

REPORT SUMMARY

A. PROGRAM SCOPE AND OBJECTIVE

This interim technical report covers the period November 24, 1977 to May 24, 1978. We report here on Defense Advanced Research Projects Agency/Office of Naval Research (DARPA/ONR) sponsored research directed towards the development of high average power rare gas monohalide laser systems applicable to specific DARPA missions. The overall objective of the One Meter Laser Research program is to: 1) identify the key physical processes governing the operation of this class of lasers, and 2) experimentally verify laser performance predictions made by laser model calculations.

In the previous reporting period the one-meter XeF laser experiments had shown that, at room temperature, the laser efficiency was limited by the rate of lower laser state removal (bottlenecking) and by the rate of vibrational relaxation in the upper state vibrational manifold. This work led to the proposal to seek improved XeF laser efficiency at elevated temperatures.

For this reporting period a major portion of the effort was devoted to installing a heated laser cell on the one-meter e-gun. This cell was then used to study XeF laser performance at elevated temperatures. A portion of the effort was also devoted to additional KrF laser experiments. Laser output energy,

pulse shape, KrF^* and Kr_2F^* sidelight emissions were measured for a range of mixtures, pressures and excitation intensities. The results of these experiments have been compared with scaling predictions made by our comprehensive KrF laser code.

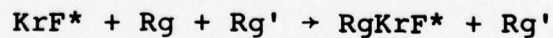
In parallel with the above, theoretical calculations were made on 1) vibrational excitation/de-excitation and dissociation rate constants for ground state XeF as functions of temperature and 2) three-body recombination rate constants of KrF^* with various rare gases.

B. ACCOMPLISHMENTS AND FINDINGS

The major results obtained in this reporting period are summarized as follows:

- 1) Construction and testing of the one-meter heated laser cell were completed.
- 2) The XeF intrinsic laser efficiency was shown to increase by more than a factor of two at elevated temperatures.
- 3) At optimum temperature an intrinsic XeF laser efficiency of 5.5% was achieved at 3 amagats.
- 4) The increase in laser efficiency was shown to be a result of improved energy extraction brought about by increased rate of lower level removal and upper state vibrational mixing.
- 5) The energy loss due to the formation of $\text{XeF}^*(\text{C})$ and excited triatomics in XeF laser mixtures was shown to be saturable by laser cavity flux.

- 6) The change in XeF laser output spectra at elevated temperatures was shown to be attributable to the increase in lower level removal and to the change in upper state rotational distribution.
- 7) The various effects of increased temperature in XeF laser kinetics have been incorporated into the comprehensive laser model.
- 8) The observed laser performance was shown to be consistent with model predictions.
- 9) KrF laser output, KrF* and Kr₂F* sidelight intensities have been compared with model predictions and shown to agree within experimental error.
- 10) KrF laser scaling projections were made.
- 11) The rates of lower state (XeF(x)) removal by vibrational mixing and dissociation have been calculated for various vibrational states and temperatures.
- 12) The rate constants for three-body recombination reactions of the type



have been calculated as functions of temperature.

C. PLANS FOR NEXT PERIOD

For the next six-month period the one-meter device will be used to study KrF laser performance at elevated temperatures. An improvement in KrF laser efficiency is expected because three-body recombination calculations indicate reduce KrF* quenching by

Kr and Ar at elevated temperatures. The one-meter device will also be used to study e-beam controlled discharge pumping of HgCl lasers. Discharge pumping of HgCl has the possibility of yielding a visible laser with intrinsic efficiency approaching 20%.

TABLE OF CONTENTS

| <u>Section</u> | | <u>Page</u> |
|----------------|--|-------------|
| | Report Summary | 1 |
| | List of Illustrations | 7 |
| I. | INTRODUCTION | 9 |
| II. | ONE-METER HEATED LASER CELL | 11 |
| III. | XeF LASER PERFORMANCE AT ELEVATED TEMPERATURES | 17 |
| | A. Heated XeF Laser Experiments | 18 |
| | B. Sidelight Measurements | 20 |
| | C. Data Interpretation | 31 |
| IV. | KrF LASER EXPERIMENTS AND COMPARISONS WITH MODEL PREDICTIONS | 39 |
| | A. KrF* Laser Kinetics | 40 |
| | B. Power Extraction | 46 |
| | C. Experimental Results and Comparison with Model Predictions | 47 |
| | D. Discussion | 52 |
| V. | THEORETICAL RATE CONSTANT CALCULATIONS | 59 |
| | A. Calculation of XeF Ground State Dissociative Rate Constants | 60 |
| | B. Temperature Dependence of KrF* Recombination Rate Constants | 68 |
| VI. | PLANS FOR NEXT PERIOD | 75 |
| | References | 77 |

LIST OF ILLUSTRATIONS

| <u>Figure</u> | | <u>Page</u> |
|---------------|--|-------------|
| 1 | One Meter Heated Laser Cell | 12 |
| 2 | Cross-Sectional View of Cell Ends | 13 |
| 3 | XeF Intrinsic Laser Efficiency vs Initial Gas Temperature | 19 |
| 4 | Laser Output Spectra at Various Temperatures | 21 |
| 5 | Fluorescence Intensity vs Temperature | 23 |
| 6 | XeF* Fluorescence Spectra at Various Temperatures | 24 |
| 7 | XeF* Sidelight Spectra with and without Laser Cavity Flux | 25 |
| 8 | Experimental Arrangement for Sidelight vs Cavity Flux Measurements | 26 |
| 9 | Ratio at Sidelight Intensities vs Cavity Flux | 28 |
| 10 | Experimental Arrangement for Measuring B \rightarrow X and Broadband Sidelight Emissions | 29 |
| 11 | B \rightarrow X and Broadband Photodiode Signals with and without Cavity Flux | 30 |
| 12 | Tentative Assignment of Dominant Laser Transitions | 35 |
| 13 | FCF Calculated by Tellinghuisen et. al. | 37 |
| 14 | Processes Included in the Model | 41 |
| 15 | Sidelight Measurement Geometry | 48 |
| 16 | Comparison of Measured and Calculated Pulse Shapes | 50 |
| 17 | E-Beam Current Pulseshape | 51 |

| <u>Figure</u> | | <u>Page</u> |
|---------------|--|-------------|
| 18 | Predicted Formation Efficiency η_F , Fluorescence Efficiency η_{FL} , Intrinsic Laser Efficiency η_{INT} and Extraction Efficiency η_{ext} | 55 |
| 19 | Predicted Laser Intrinsic Efficiency Scaling Characteristics | 56 |
| 20 | Calculated Dissociative Rate Constants for Various XeF Vibrational Levels | 65 |
| 21 | Calculated Recombination Rate Constant vs Temperature R = Ar | 70 |
| 22 | Calculated Recombination Rate Constant vs Temperature R = Kr | 71 |

I. INTRODUCTION

The overall objective of the DARPA/ONR sponsored rare gas monohalide laser program is to determine whether this class of lasers can be made both efficient and scalable to high average powers needed for achieving specific DARPA goals. In order to meet this objective various parts of the underlying physics governing these lasers are resolved on small scale devices. These experiments provide the various parameter values (cross sections, rate constants, etc.) which are used to develop comprehensive laser models. One-meter laser experiments are performed to first help identify the key processes that must be correctly modeled and, second, to experimentally verify that performance predictions made by model calculations can be achieved. Once the predictive capability of the models has been demonstrated then these laser models can be used to accurately assess the performance achievable with larger scale versions of these lasers.

In the previous reporting period one-meter XeF laser experiments had shown that, at room temperature, the laser efficiency was limited by the rate of lower laser state removal (bottlenecking) and by the rate of vibrational relaxation in the upper state vibrational manifold. Since both of these rates are expected to increase with temperature, we proposed to study XeF laser performance at elevated temperatures.

During this reporting period a heated laser cell was installed on the one-meter device. This cell was then used to study heated XeF laser performance. In Section II of this report the design and construction of the heated cell and its associated temperature controls and gas handling systems are described. The results of heated XeF laser experiments are presented in Section III.

In parallel with the construction of the heated cell, the one-meter device was used to perform further KrF laser experiments. The results of these experiments, together with detailed comparisons with comprehensive KrF laser model predictions are discussed in Section IV.

Also during this reporting period, theoretical calculations were carried out on (1) vibrational excitation/de-excitation and dissociation rate constants for ground state XeF as functions of temperature and (2) three-body recombination rate constants of KrF* with various rare gases. These rate constants are needed for the modeling of KrF lasers. The results of these calculations and their implications on the laser performance are described in Section V. Finally, in Section VI, plans for the next six-month period are presented.

II. ONE METER HEATED LASER CELL

In order to study the performance of rare gas monohalide lasers at elevated temperatures, a one-meter heated laser cell was designed and constructed. This cell will also be used to study e-beam controlled discharge pumping of HgCl lasers in the next reporting period. A cross-sectional view of the cell is shown in Figure 1. The cell was designed to automatically maintain a pre-selected temperature ranging from room temperature to 250°C with overall wall temperature uniformity of $\pm 5^\circ\text{C}$.

The cell is constructed of stainless steel. The cell walls are heated by electrical strip heaters. For temperature uniformity 1/4-in. aluminum plate cladding is used on the cell walls. The beam collector/discharge cathode is held in place with 3 ceramic standoffs. These are separately heated by electrical coil heaters. The ends of the cell and window holders are heated by electrical tape heaters.

Thermal insulation between the cell and the e-gun chamber is provided by a thin cross-section (1/8 in.) 2-in. wide stainless steel standoff. The cell is insulated from the surroundings by 2-in. thick Fiberfrax insulation. The spaces between the cavity windows and the optical cavity mirrors are enclosed by heated shrouds. A cross-sectional view of the cell ends is shown in Figure 2.

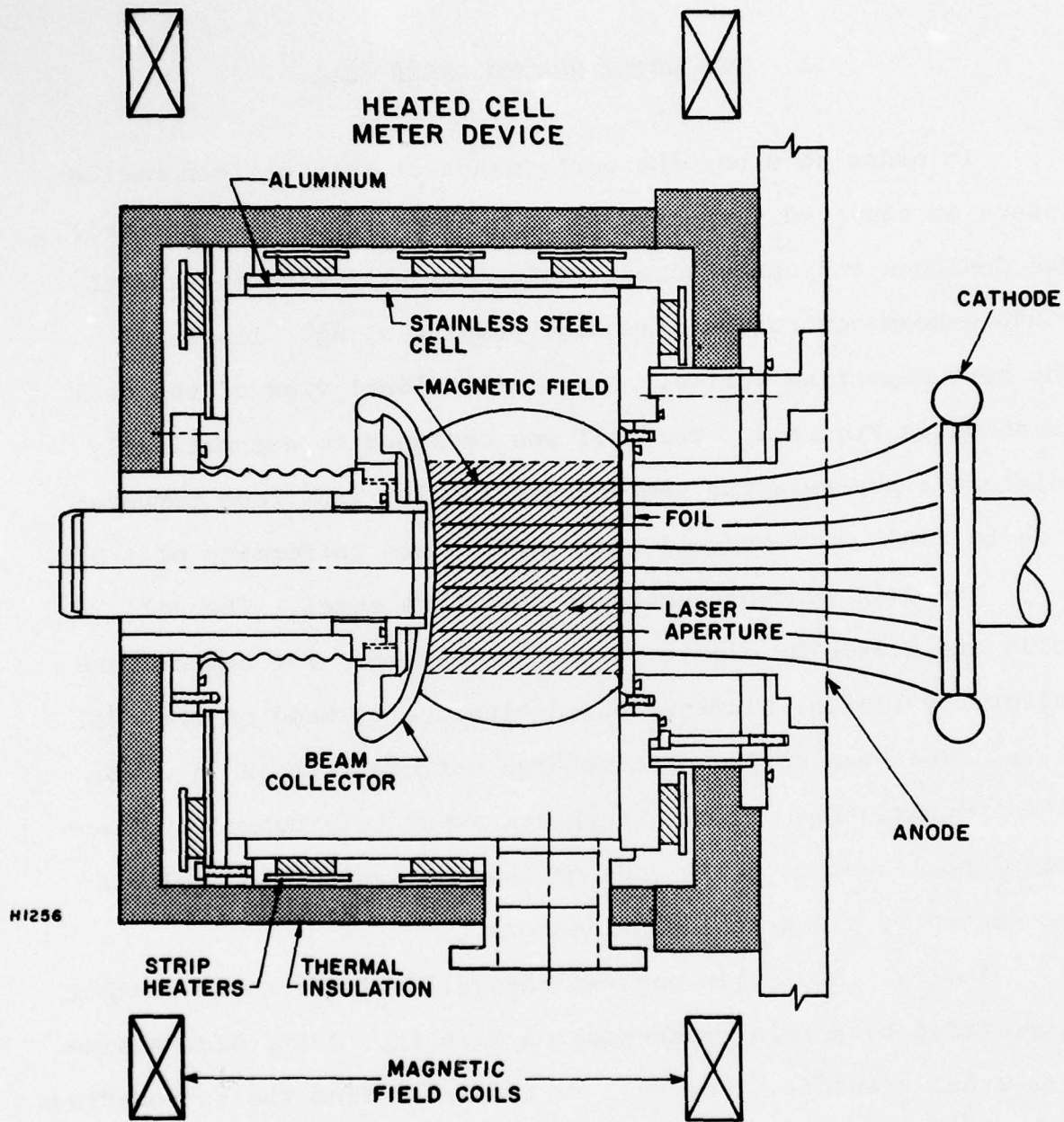


Figure 1. One Meter Heated Laser Cell

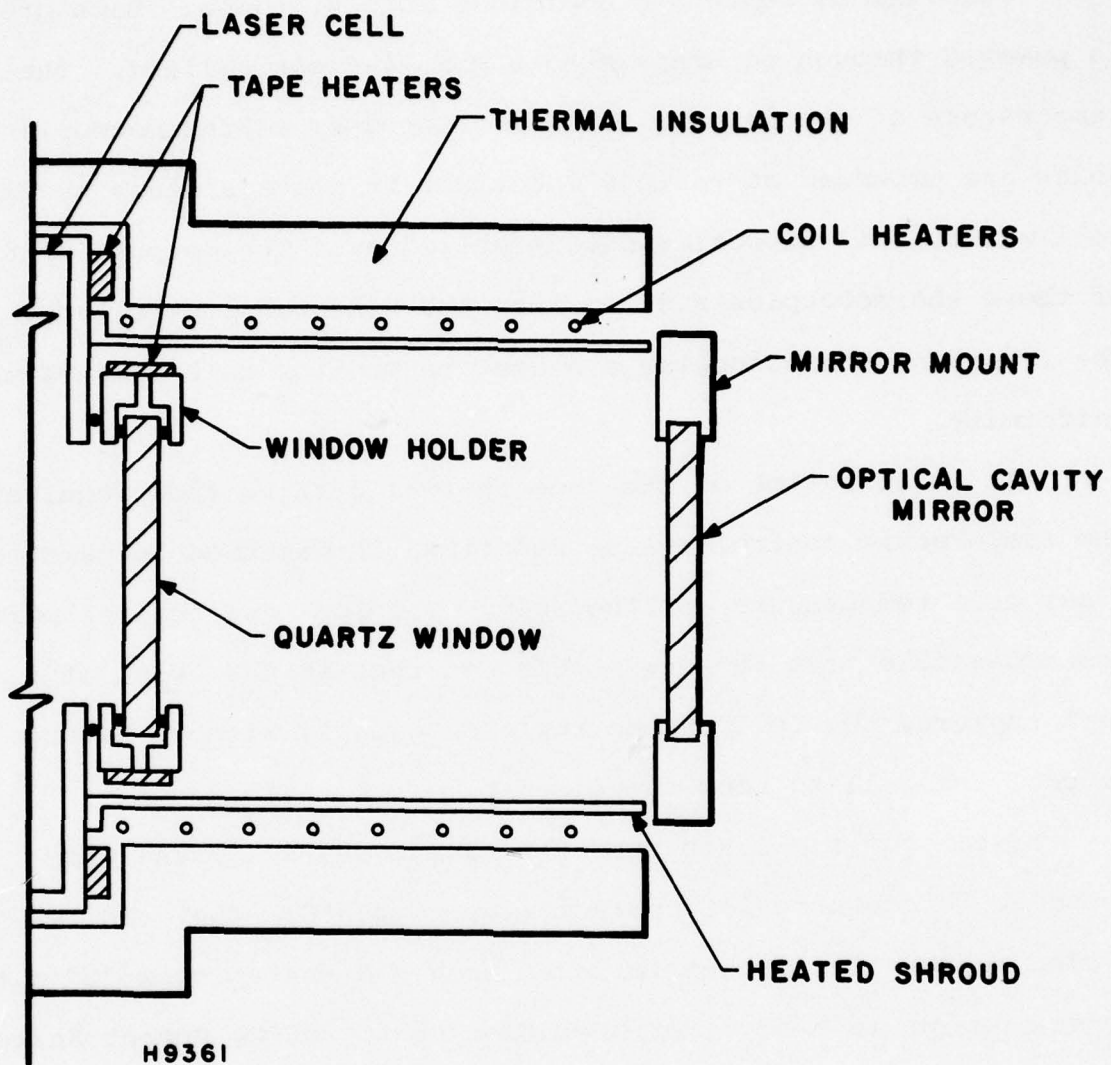


Figure 2. Cross Sectional View of Cell Ends

The various heaters are divided into 8 groups. Each group is powered through separate Athena Mod 74-6 controllers. The temperature of the cell walls is monitored by 40 thermocouples which are embedded at various locations in the stainless steel cell walls, foil support and beam collector. The outputs of 8 of these thermocouples are fed into the 8 heater controllers. The remaining thermocouples are used to monitor cell temperature uniformity.

In anticipation of the long thermal cycling time required, the temperature control system described is designed to maintain a set cell temperature continuously. The foil and foil support are accessible from the e-gun side, so that in the event of a foil rupture, the foil can be replaced quickly without having to cool the cell to room temperature.

Viton "O" rings are used for vacuum seals. These were found to be adequate for operation up to 250°C. They can be cycled repeatedly without failure, provided that proper "O" ring groove design is used. For operation up to 300°C, Dupont Kalraz "O" rings were found to provide satisfactory service.

Temperature uniformity of the cell wall was checked up to 300°C. After a few iterations on the placement of heater controlling thermocouples, $\pm 5^\circ\text{C}$ uniformity was achieved over the entire cell. Temperature of the quartz windows was measured using thermopaint. During heat-up the window temperature lagged considerably behind the cell temperature, due to the poor thermal

conductivity of quartz. With 1 atm of He in the cell, the center of the quartz window reached operating temperature some 3 hr after equilibrium was attained on the cell walls. This problem can be alleviated by the use of heat lamps on the windows.

The laser gas mixture is stored premixed in heated storage cylinders. The gas is introduced into the laser cell via a heated tube. In anticipation of spontaneous wall reactions problems between Hg and Cl₂ in HgCl laser mixtures (also possible reaction of halogen donor in rare gas halide mixtures with cell walls), the cell walls, gas storage tanks and feed tubes were all coated with high temperature teflon.

III. XeF LASER PERFORMANCE AT ELEVATED TEMPERATURES

In the previous reporting period, using e-beam excitation, we were able to achieve an intrinsic XeF laser efficiency of 2.6%. Laser sidelight measurement had shown that the efficiency was severely limited by the rate of vibrational mixing in the XeF*(B) vibrational manifold and by the rate of XeF(x) removal.

Preliminary calculations of the rate of XeF(x) removal via collisional excitation and dissociation indicated that this rate should increase dramatically with modest increases in temperature. For example, at 450°K the theory predicted a factor of 3 increase in the dissociation rate constant compared with room temperature. This increase is expected to yield a 60% increase in laser efficiency. The theory also indicated that the temperature dependence is stronger for lower vibrational levels of XeF(x). Therefore, heating may lead to strong lasing in the $v' = 0 \rightarrow v'' = 2$ transition at 3511 Å. Lasing in this transition would also result in extraction from the $v' = 1$ level in the upper state because the $v' = 1 \rightarrow v'' = 4$ transition is coincident in wavelength with the $0 \rightarrow 2$. Furthermore heating may also increase the rate of vibrational relaxation in the XeF*(B) vibrational manifold. If this increase is sufficiently large, then lasing in one $v' \rightarrow v''$ transition can extract energy from other v' levels through vibrational relaxation. All these effects

combined are expected to improve the laser efficiency of more than a factor of two.

In this section we first report on the result of heated laser experiments. Then we report on sidelight experiments performed to study the mechanisms leading to the observed improvement in laser efficiency and output spectra.

A. HEATED XeF LASER EXPERIMENTS

The intrinsic laser efficiency was measured vs temperature for 2 and 3 amagat gas densities. The results are shown in Figure 3 where we have plotted the measured intrinsic efficiency vs initial gas temperature. The efficiencies shown were derived by dividing the measured laser energy out by the measured e-beam energy deposited in the laser mixture. Methods of e-beam and laser energy measurements were described in the previous report. (1) For these measurements the gas mixture was kept constant at 0.1% NF_3 /0.5% Xe/99.4% Ne. The optical cavity output couplings were 44% and 84% for 2 and 3 amagat, respectively. These were found to be approximately optimal for the respective operating conditions. For each density the only parameter varied was the initial gas temperature.

As the temperature was raised the laser efficiency first increased with temperature until an optimum point was reached. Further heating resulted in a drop in efficiency. The highest laser efficiency was 5.5%, which was obtained at 450°K and 3 amagats gas density. This was a factor of 3 higher than that

(1) Hsia, J.C., Mangano, J.A., Jacob, J.H., Rokni, M., "One-Meter KrF Laser System," Semi-Annual Report, Feb. 23, 1977 to Aug. 22, 1978.

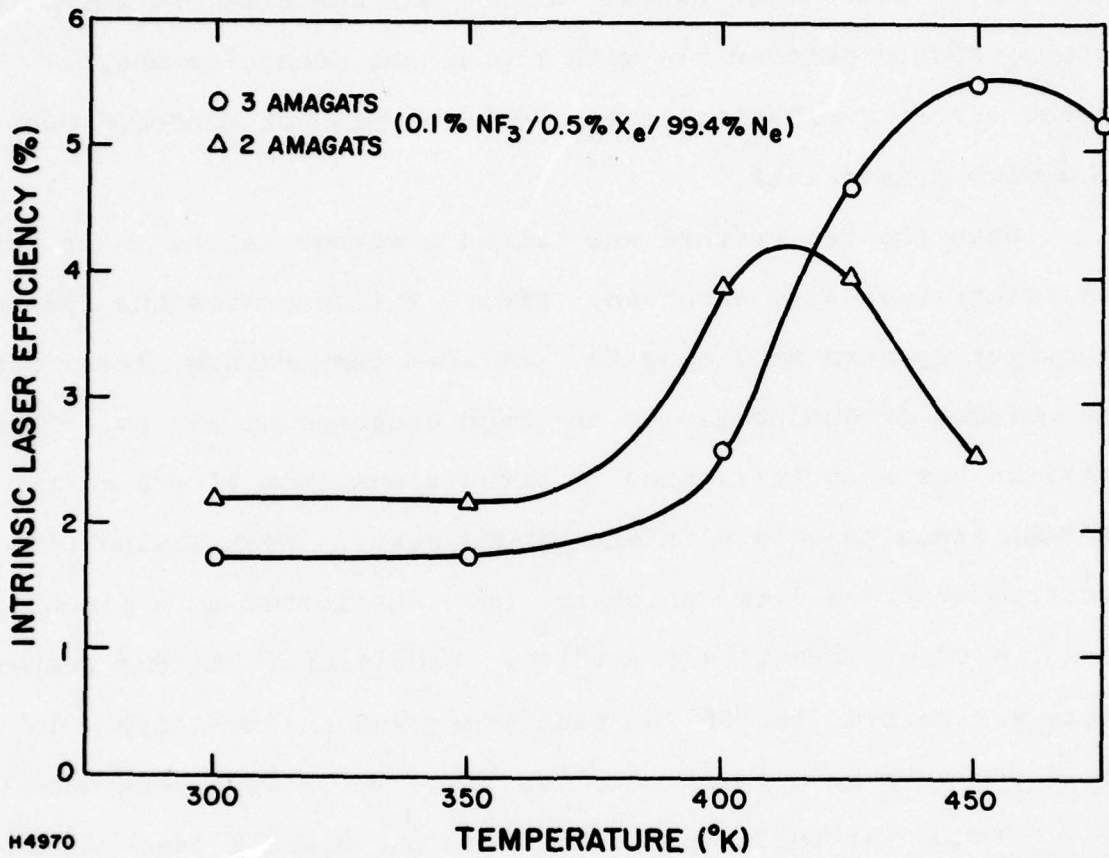


Figure 3. XeF Intrinsic Laser Efficiency vs Initial Gas Temperature

observed at 300°K under otherwise identical conditions. The associated volumetric laser output was 5 J/l, which was extracted in a 750 nsec laser pulse. Higher efficiencies and volumetric outputs should be possible with higher gas densities and/or higher e-beam excitation levels. These were not explored due to device constraints.

When the temperature was raised a change in the laser output spectra was also observed. Figure 4 illustrates the change in output spectra at 2 amagats. At room temperature, laser power was emitted predominantly in the band centered at 353 nm. This emission has been attributed to transitions from $v' = 0$ in the $\text{XeF}^*(\text{B})$ state to $v'' = 3$ in the ground state. Weak lasing also occurred around 351 nm, which has been attributed to a blend of $v' = 1 \rightarrow v'' = 4$ and $v' = 0 \rightarrow v'' = 2$ transitions. As the temperature was raised, the 351 nm band increased in intensity. In addition, this band split into two peaks which were separated by ~ 0.1 nm. At the temperature where the highest laser efficiency was observed, both the band at 353 nm and the two bands around 351 nm were lasing strongly. Further heating led to a decrease in laser output in the 353 nm band.

B. SIDELIGHT MEASUREMENTS

In order to study the physical processes leading to the observed improvement in laser efficiency and change in output spectra, sidelight measurements were carried out at various temperatures. Measured were relative sidelight fluorescence intensities and spectra vs temperature both with and without the presence of a laser cavity flux.

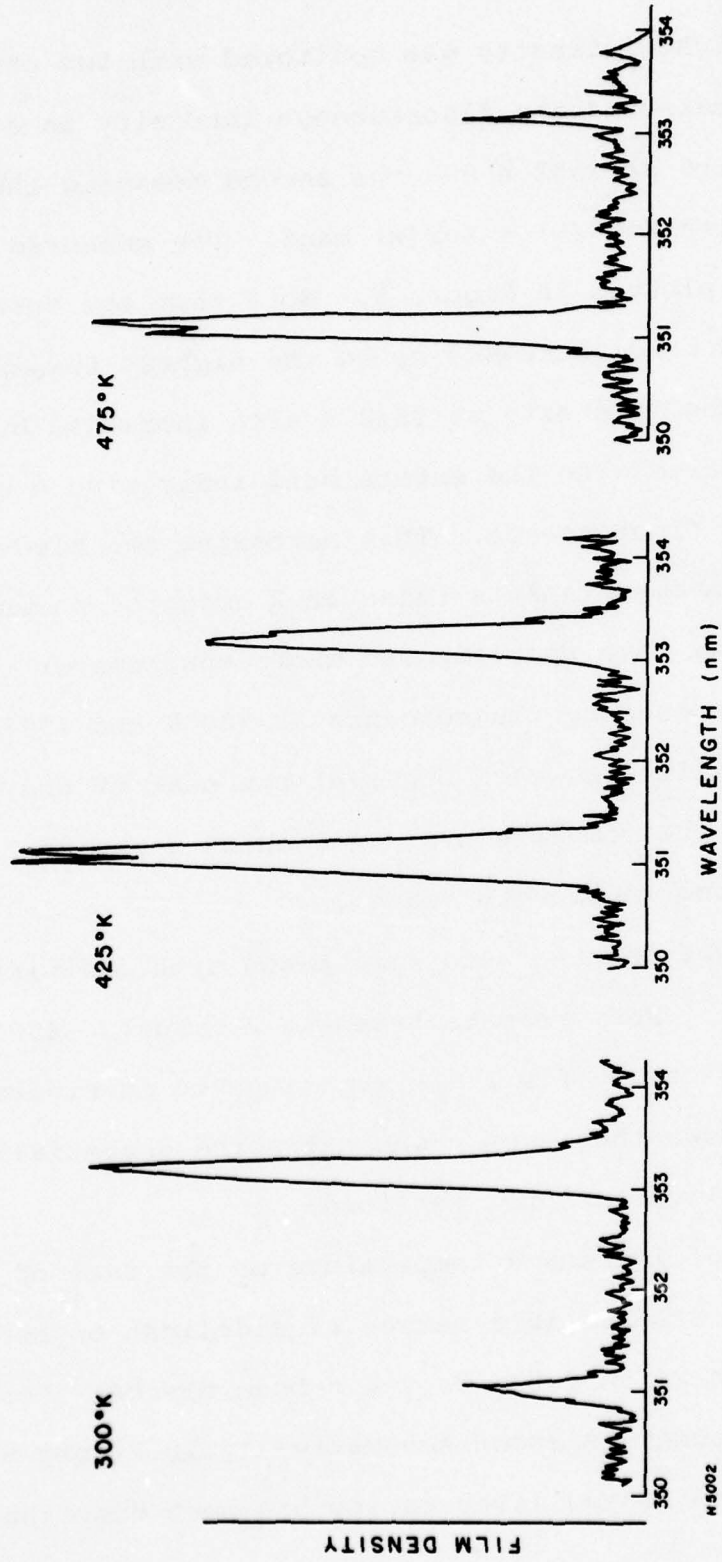


Figure 4. Laser Output Spectra at Various Temperatures

The sidelight intensity was monitored with two photodiodes. One photodiode measured the fluorescence intensity in a 10 Å FWHM band centered at 3532 Å and the second measured the intensity in the entire XeF*(B) → XeF(x) band. The measured relative intensities are plotted in Figure 5. Note that the intensity in the entire B → X band increased up to the highest temperature investigated. The intensity at 3532 Å also increased but at a faster rate compared with the entire band indicating a spectral narrowing of the fluorescence. This narrowing can also be seen from spectrograph measurements taken at 2 amagats, shown in Figure 6. Here we have superimposed microdensitometer tracings of film plates exposed by fluorescence at 300°K and 450°K. The traces were normalized to each other at the peak of the 3532 Å line. Note that the comparison clearly shows a spectral narrowing toward the long wavelength region.

The sidelight spectra were also taken with and without a laser cavity flux. Measurements taken at 2 amagats, 450°K with and without laser cavity flux, are superimposed in Figure 7. The comparison shows that energy was extracted essentially from the entire XeF*(B) vibrational manifold.

The effect of increased temperature on the rate of lower level removal was studied in a series of sidelight experiments carried out on the 20 cm cable-driven e-beam device. The experimental arrangement is shown schematically in Figure 8. The 20 cm e-gun and heated laser cavity has been described

XeF* B→X FLUORESCENCE vs TEMPERATURE
(0.1% NF₃/0.5% Xe/99.4% Ne AT 2 AMAGATS)

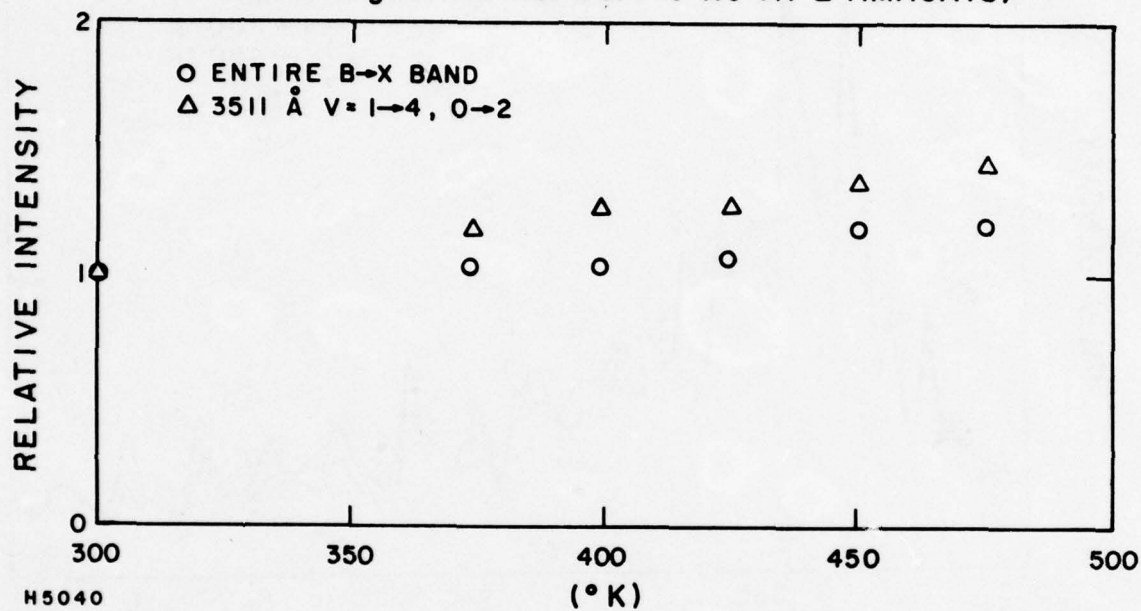


Figure 5. Fluorescence Intensity vs Temperature

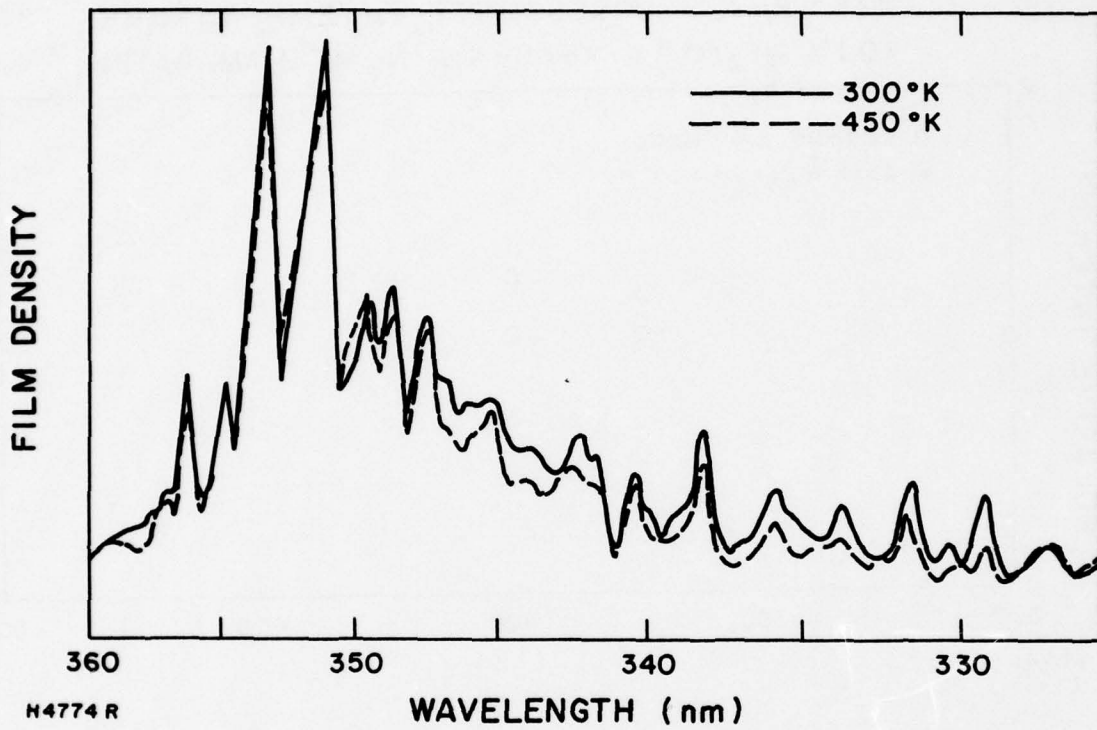


Figure 6. XeF* Fluorescence Spectra at Various Temperatures

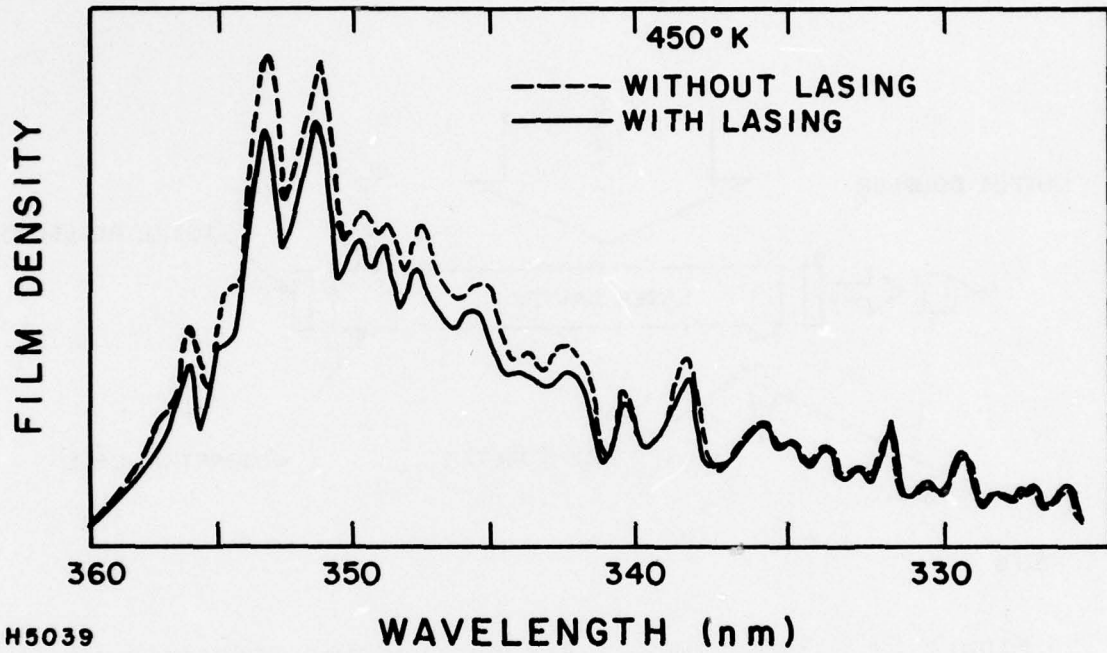
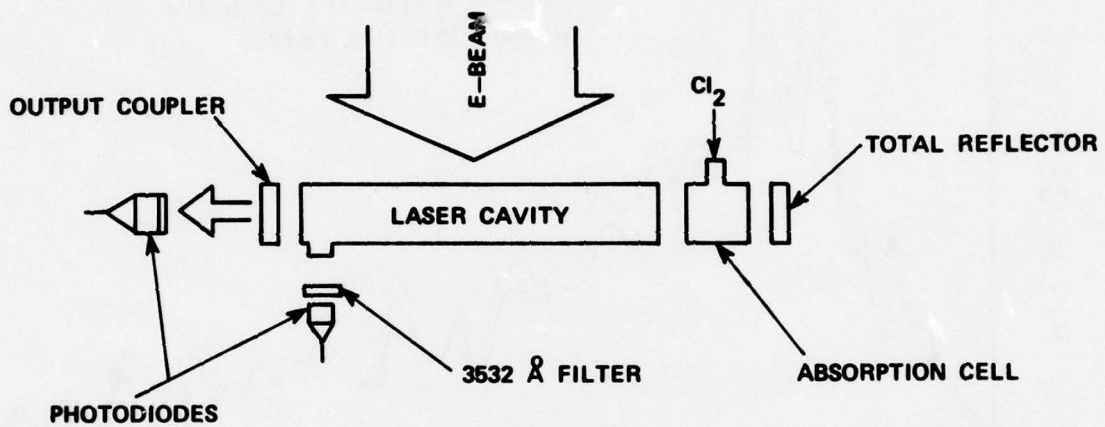


Figure 7. XeF* Sidelight Spectra with and without Laser Cavity Flux



H5178

Figure 8. Experimental Arrangement for Sidelight vs Cavity Flux Measurements

previously.⁽²⁾ A quartz absorption cell was inserted into the optical resonator formed by a max reflector ($R = 99\%$) and a 4% transmitting output coupler, so that the Q of the resonator (and therefore the cavity flux) could be continuously varied for fixed excitation conditions, by varying the Cl_2 pressure in the quartz cell. The laser output flux in the 3532 \AA band was monitored by a calibrated photodiode. The cavity flux inside the resonator near the output coupler can be calculated from the output flux using the measured transmittance and reflectivity of the output coupler. The sidelight, within a 10 \AA wide band centered about 3532 \AA , emitted close to the output coupler was monitored by another photodiode.

The ratios of sidelight intensities with no cavity flux to that with cavity flux ϕ are plotted in Figure 9 vs ϕ for 300°K and 475°K initial gas temperatures.

Sidelight experiments were also performed to study the kinetics of excited species ($XeF^*(C)$ or triatomic $NeXeF^*$) formation in XeF^* laser mixtures leading to broadband emission centered around 460 nm . The experimental arrangement used is shown schematically in Figure 10. Sidelight intensities were measured in the 300 nm to 380 nm ($XeF^*(B \rightarrow X)$), and 400 nm to 600 nm bands. Typical photodiode signals are shown in Figure 11.

(2) Mangano, J.A. and Jacob, J.H., Appl. Phys. Lett. 27, 495 (1975).

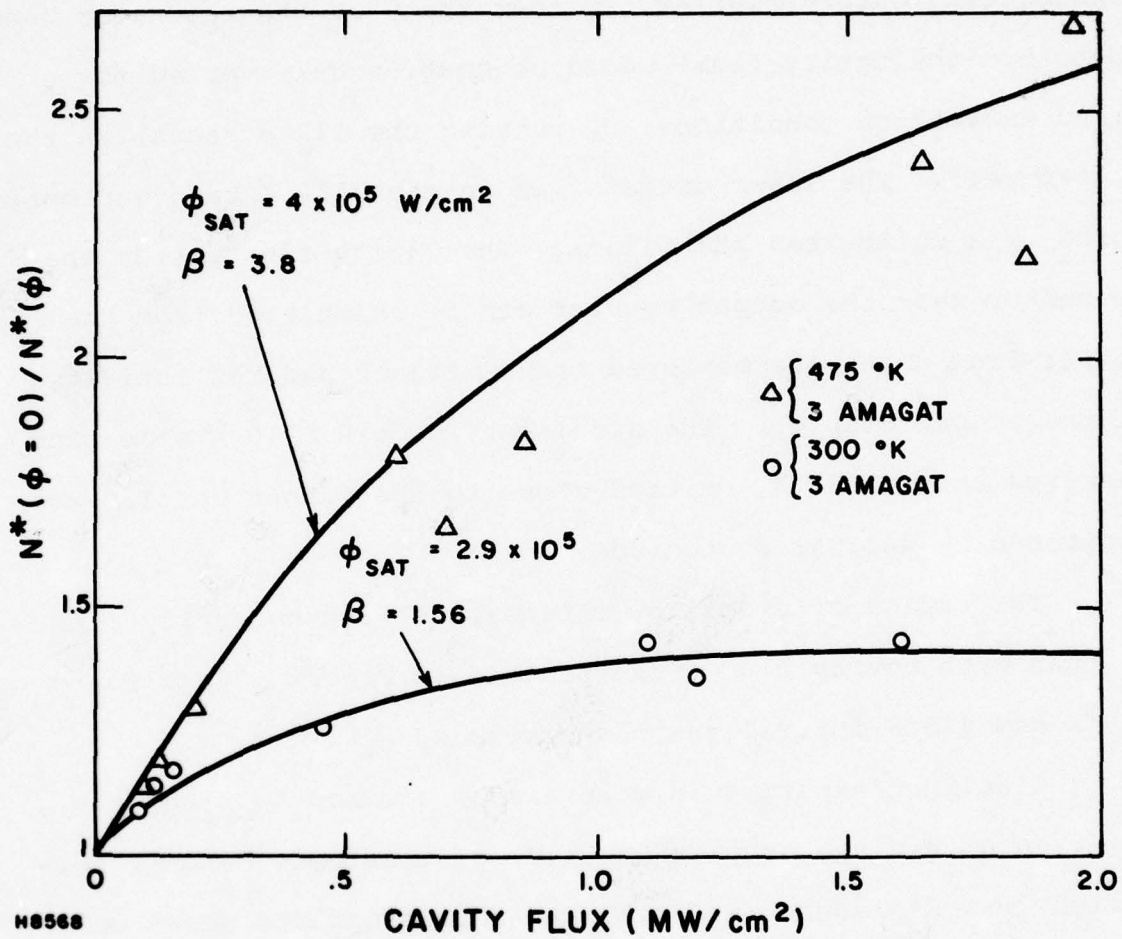


Figure 9. Ratio at Sidelight Intensities vs Cavity Flux

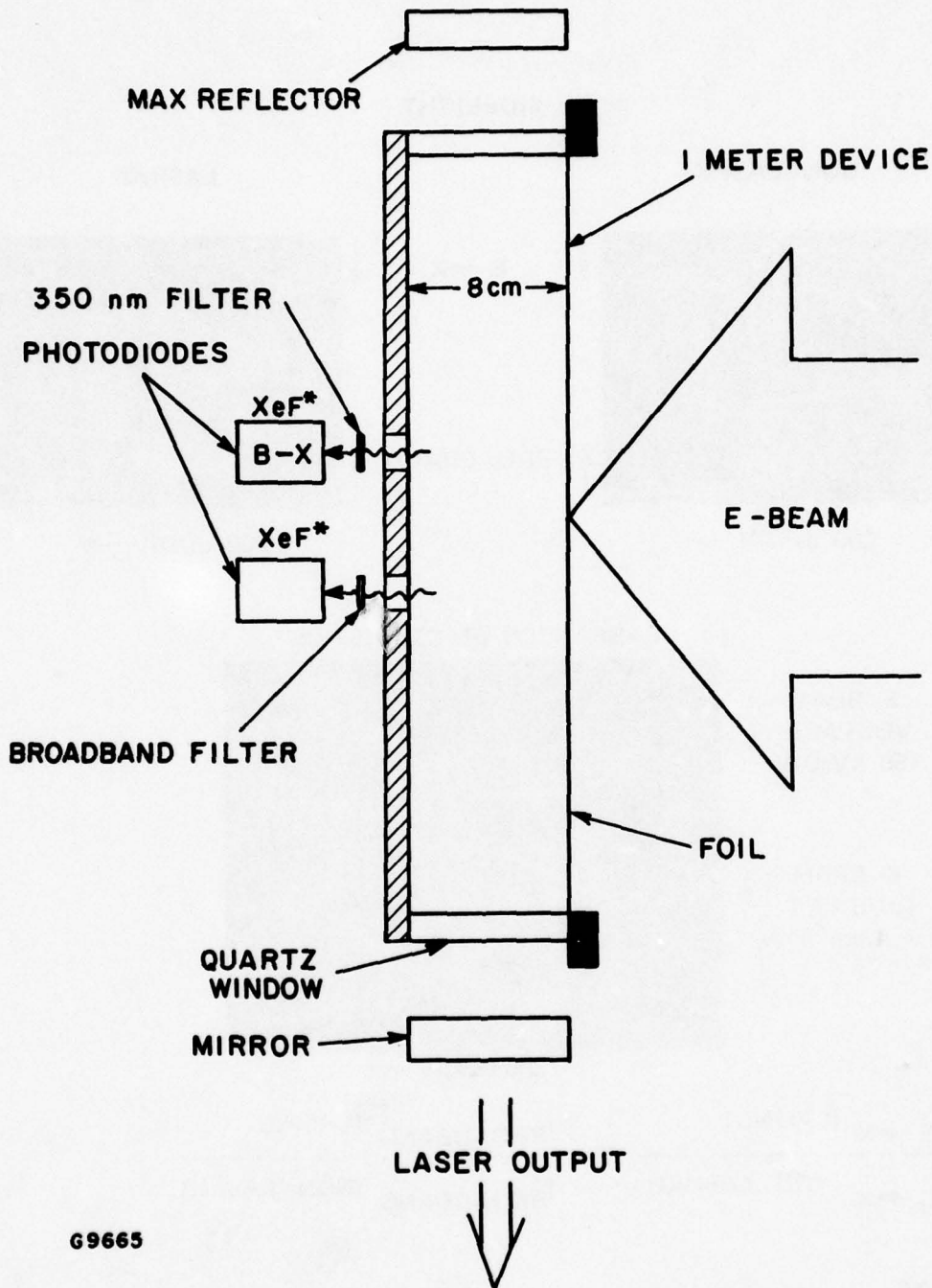
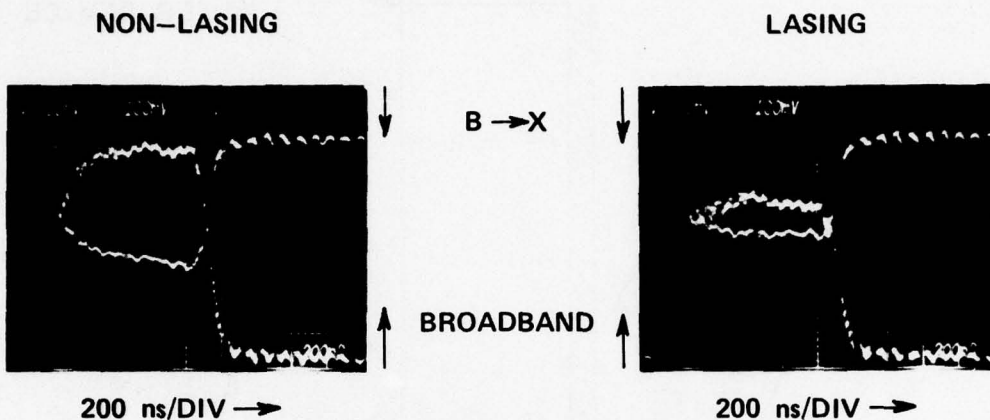


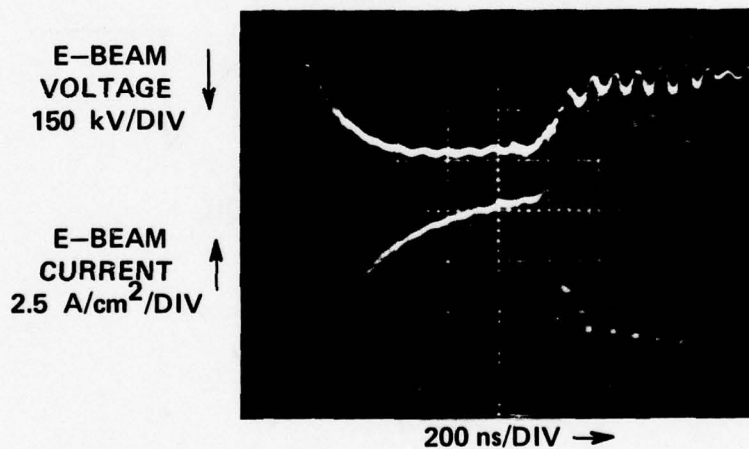
Figure 10. Experimental Arrangement for Measuring B \rightarrow X and Broadband Sidelight Emissions

(Ne DILUENT, 2 ATM)

SIDELIGHT



E-BEAM CHARACTERISTICS



$$\frac{I_{B \rightarrow X} \text{ (LASING)}}{I_{B \rightarrow X} \text{ (NON-LASING)}} \approx \frac{I_{\text{BROADBAND}} \text{ (LASING)}}{I_{\text{BROADBAND}} \text{ (NON-LASING)}}$$

H7025

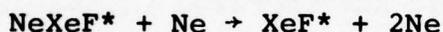
Figure 11. B → X and Broadband Photodiode Signals with and without Cavity Flux

C. DATA INTERPRETATION

The increase in fluorescence intensity with temperature over the entire (XeF*(B → X) band can be attributed to slightly reduced quenching of XeF*. This reduction may be due to a reduction in the rate of three-body quenching reaction



A reduction in rate of this reaction can be expected if NeXe⁺ is very slightly bound. In this case an increase in temperature would be expected to favor the reverse reaction



Another possibility is that the dissociative electron attachment rate constant of NF₃ increases with temperature. In this case heating would lead to a lower electron density and thereby reduce the electron quenching of XeF*. Small scale experiments will be performed in the next reporting period to study these processes.

The narrowing of the fluorescence spectra shown in Figures 5 and 6 can be attributed to an increase in the rate of vibrational relaxation in the XeF*(B) vibrational manifold. At room temperature the density distribution in the XeF*(B) vibrational levels is not fully relaxed. Evidence for this was presented in the previous interim report.⁽¹⁾ An increase in the vibrational relaxation rate brought about by heating would drive the distribution closer to equilibrium which, in this case, would lead to an increase in the relative population of the lowest vibrational levels and thus result in the observed change in fluorescence spectrum.

The sidelight spectra shown in Figure 7 indicate that at 450°K where the highest laser efficiency was achieved, the laser cavity flux extracted energy from essentially the entire XeF*(B) vibrational manifold. This increase in extraction efficiency with temperature can be attributed to two causes. First is that at 450°K strong laser action occurred in $v = 0 \rightarrow 3$, $0 \rightarrow 2$, and $1 \rightarrow 4$ transitions; therefore, the laser cavity flux directly stimulated XeF* in both the $v' = 0$ and $v' = 1$ levels. Whereas, at room temperature, strong lasing occurred only from XeF* $v' = 0$ level. Second is that the increase in the vibrational mixing rate at elevated temperatures lead to increased feeding of XeF* from $v' \geq 2$ levels into the $v' = 0$ and 1 levels where extraction by the cavity flux occurred. The combination of these effects lead to efficient extraction from the entire XeF*(B) vibrational manifold.

The extraction efficiency is also increased by an increase in the rate of lower level removal as demonstrated by the data shown in Figure 9. Quantitatively, we can estimate the increase in this rate as follows. Consider the steady state rate equations for the upper and lower levels

$$\frac{dN^*}{dt} = S - \frac{\phi\sigma_s}{h\nu} (N^*-N) - \frac{N^*}{\tau_s} - \frac{N^*}{\tau_Q} = 0 \quad (1)$$

$$\frac{dN}{dt} = \frac{\phi\sigma_s}{h\nu} (N^*-N) + \frac{N^*}{\tau_s} - \frac{N}{\tau_L} = 0 \quad (2)$$

where N , N^* are the lower and upper level number densities. ϕ is the laser cavity flux. τ_s , τ_Q and τ_L are the XeF* spontaneous lifetime, the quenching lifetime and the lower level lifetime respectively. σ_s is the stimulated emission cross section and S is the upper level pumping rate.

These equations yield

$$\frac{N^*(\phi=0)}{N^*(\phi)} = \frac{1 + \frac{\phi}{\phi_s}}{1 + \frac{1}{\beta} \frac{\phi}{\phi_s}} \quad (3)$$

where

$$\phi_s = \frac{h\nu}{\sigma_s \tau} \left(\frac{1}{1 + \frac{\tau_L}{\tau} - \frac{\tau_L}{\tau_s}} \right)$$

$$\beta = 1 + \frac{\tau}{\tau_L} - \frac{\tau}{\tau_s}$$

$$\tau = \frac{\tau_s \tau_Q}{\tau_s + \tau_Q}$$

τ_Q can be calculated from measured quenching rate constants. Taking a σ_s of $2 \times 10^{-16} \text{ cm}^2$, τ_s of 16 nsec, one can fit the data points shown in Figure 9 with Eq. (3) by adjusting the only remaining free parameter τ_L . The data points, together with best fit curves, are shown in Figure 10. These curves yield

$$\tau_L = 6.2 \text{ nsec} \quad 300^\circ\text{K}$$

$$\tau_L = 1.8 \text{ nsec} \quad 475^\circ\text{K}$$

respectively. These agree well with our preliminary calculations on the temperature dependence of XeF dissociation. If this change

in lower state lifetime is included in the model calculations, then the model predicts a 55% increase in extraction efficiency at 475°K compared with 300°K for the conditions of 3 amagat experiments shown in Figure 3. This, together with the increase in extraction from the higher v' levels in XeF* previously discussed, imply that one can expect a total intrinsic efficiency improvement of a factor of 2.6.

Aside from the improvement in the intrinsic laser efficiency, the physical processes leading to the observed changes in laser output spectra and to the eventual decrease in laser efficiency at temperatures $> 475^\circ\text{K}$, remain to be identified. Some plausible processes are suggested below.

As the temperature was raised, the laser emission at 3511 Å increased dramatically in intensity. In addition, a new peak ~ 1 Å to the blue of the 3511 Å peak appeared. The wavelength separation of the two peaks is close to the calculated separation between the $v = 0 \rightarrow 2$ and $v = 1 \rightarrow 4$ transition bandheads.⁽³⁾ If we tentatively identify the emission features as shown in Figure 12, then the new peak found at elevated temperatures can be attributed to lasing in the $v = 0 \rightarrow 2$ transition. This transition is expected to be strongly favored by heating for two reasons. First, the lower laser level $v'' = 2$ is more strongly bound compared with $v'' = 3$ and 4, and the rate for its deactivation, via vibrational

(3) Smith, A.L., Kobrinsky, P.C., J. Mol. Spect. 69, 1 (1978).

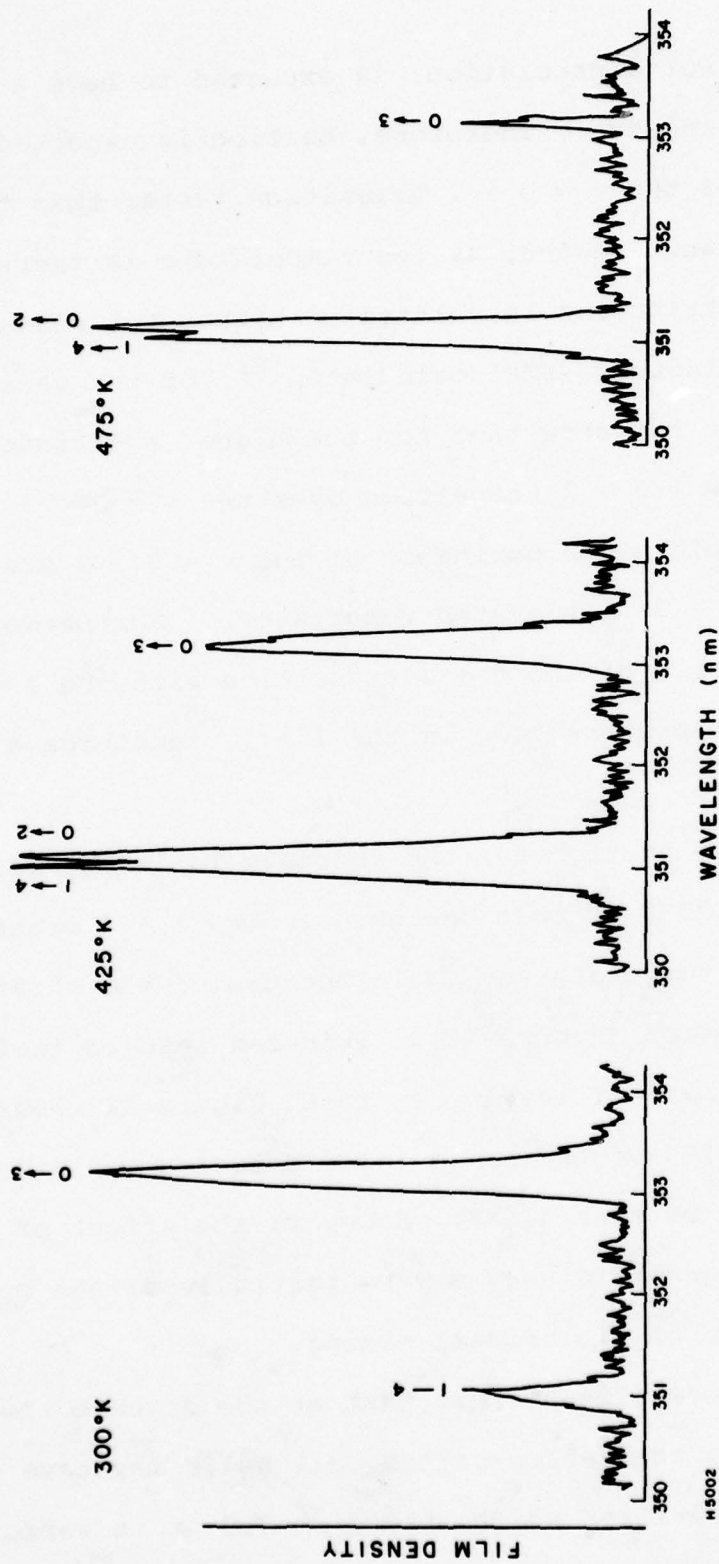


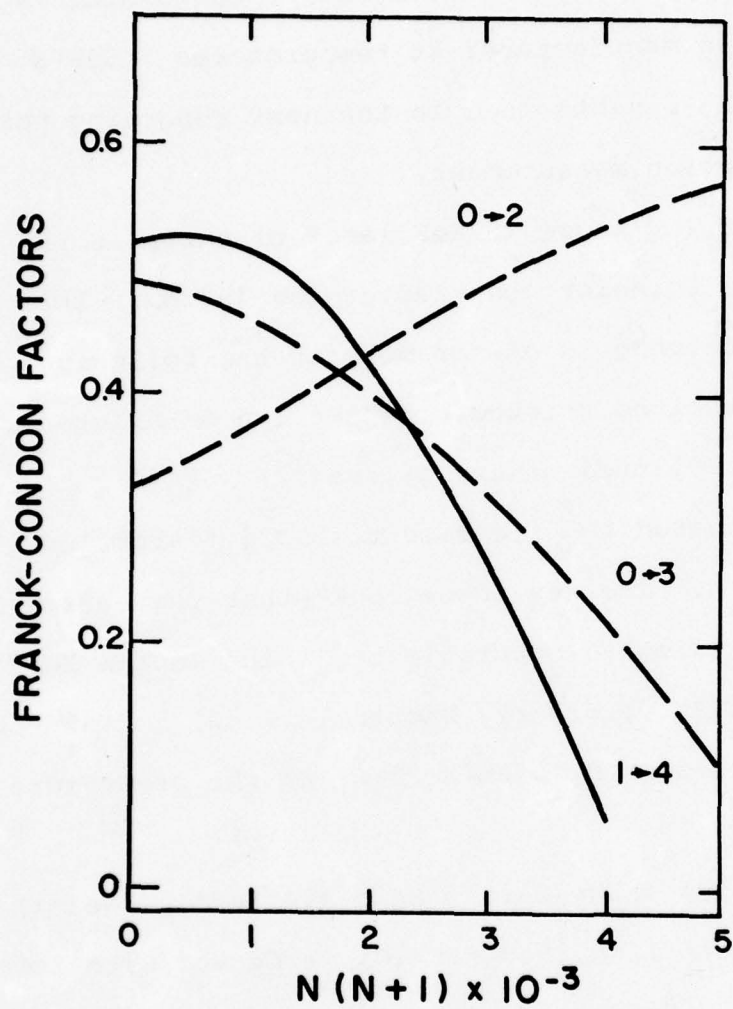
Figure 12. Tentative Assignment of Dominant Laser Transitions

excitation and direct dissociation, is expected to have a stronger temperature dependence. Therefore, heating is expected to increase the gain of the $v = 0 \rightarrow 2$ transition faster than the $v = 0 \rightarrow 3$ transition. Second, as the temperature is increased the rotational distribution is shifted to higher rotational states. The Franck Condon factors (FCF) calculated⁽⁴⁾ for the various transitions (Figure 13) show that for the higher rotational states the FCF favor the $v = 0 \rightarrow 2$ transition over the $v = 0 \rightarrow 3$. These two effects may explain the dominance of the $v = 0 \rightarrow 2$ transition over that of $v = 0 \rightarrow 3$ at elevated temperature. Furthermore, the close wavelength match of the $0 \rightarrow 2$ transition with the $1 \rightarrow 4$ transition means that extraction in the $1 \rightarrow 4$ transition also becomes more efficient.

A possible explanation for the decrease in laser efficiency at temperatures $> 475^\circ\text{K}$ is that the gain in the $1 \rightarrow 4$ transition decreased at these temperatures, again because of the shift in rotational distribution (Figure 13). This can lead to inefficient extraction from the $v' = 1$ level. In fact, Figure 12 shows that the relative intensity of the $1 \rightarrow 4$ laser emission again decreased at temperatures higher than 475°K . However, the effect of this on overall extraction efficiency may be partially offset by the increase in the rate of vibrational mixing.

An alternative explanation is that at the highest temperature outgassing from the teflon-coated cell walls may have introduced sufficient impurities which absorb at 350 nm to seriously

(4) Tellinghuisen, P.C., et al., J. Chem. Phys. 68, 5187 (1978).



TELLINGHUISEN ET AL, J. CHEM. PHYS.

H5589

Figure 13. FCF Calculated by Tellinghuisen et. al.

affect laser performance. Substantial outgassing is expected by the coating manufacturer at temperatures $> 500^{\circ}\text{K}$. This possibility will be investigated in the next reporting period by direct absorption measurement.

Another key issue in XeF laser mixtures is the origin of the broadband emission centered around 460 nm. This emission can be attributable to one or more of the following: 1) XeF* (C \rightarrow A), 2) excited triatomic NeXeF* (in Ne-diluted mixtures) or ArXeF* (in Ar-diluted mixtures), and 3) XeF*(B \rightarrow A). All the above are expected to give rise to broad featureless emission in the blue-green. The key issue is whether the energy loss to this broadband emission is saturable by lasing in the XeF*(B \rightarrow X) transition. (3) is clearly saturable. (2) is saturable if the triatomics are formed, with XeF*(B) as the precursor, through the reactions



(1) is saturable if either XeF*(C) is formed with XeF*(B) as the precursor or if XeF*(C) is well mixed with XeF*(B) by collisions.

The data shown in Figure 10 clearly demonstrate that the loss is saturable. Note that the sidelight depression in the broadband is the same as that in the B \rightarrow X, therefore, lasing in the B \rightarrow X band reduces the loss to broadband emission in the same ratio as that due to quenching and spontaneous emission of XeF*(B). This means that, except for a reduction in small signal gain on the XeF*(B \rightarrow X) transition, the formation of broadband emitting species can be neglected.

IV. KrF LASER EXPERIMENTS AND COMPARISONS WITH MODEL PREDICTIONS

The physical processes which determine the performance of KrF* lasers have been intensively researched during the last two years. As a result of this research, for e-beam excitation intensities in the $1-5 \times 10^5$ W/cm² regime, the dominant formation and quenching kinetics are well understood,^(5,6) the stimulated cross section has been measured, and the dominant absorbers in the active medium has been identified.⁽⁷⁾ The above information allows one to construct a comprehensive model which can be used to predict laser performance over a wide range of laser operating conditions. An experimental verification of the predictive capability of such a model then provides an independent check on the various kinetics leading to medium gain and absorption, as well as a check on the validity of power extraction model.

In this section, a description of such a code is presented. The predictions of the code are compared with experimental results obtained with the 1-m laser device. The comparison includes the temporal shape of the KrF* laser output and sidelight pulses, the output pulse energy, and intrinsic laser efficiency. From such a detailed comparison, it is apparent that there are processes

(5) Rokni, M., Jacob, J.H. and Mangano, J.A., Phys. Rev. A16, 2216 (1977).

(6) Velazco, J.E., Kolts, J.H. and Setser, D.W., J. Chem. Phys. 65, 3468 (1976).

(7) Hawryluk, A.M., Mangano, J.A. and Jacob, J.H., Appl. Phys. Lett. 31, 164 (1977).

that have not previously been addressed. These processes include (a) electron quenching of KrF^* , and (b) the effects of vibrational relaxation and perhaps rotational relaxation on the saturation flux and extraction efficiency.

In this section we first discuss how these kinetics are coupled to power extraction by the laser cavity flux. The detailed comparisons between the experimental results and model predictions are presented. Finally, a discussion of the processes not previously investigated will be addressed, and a scaling map for the KrF^* laser is also described.

A. KrF^* LASER KINETICS

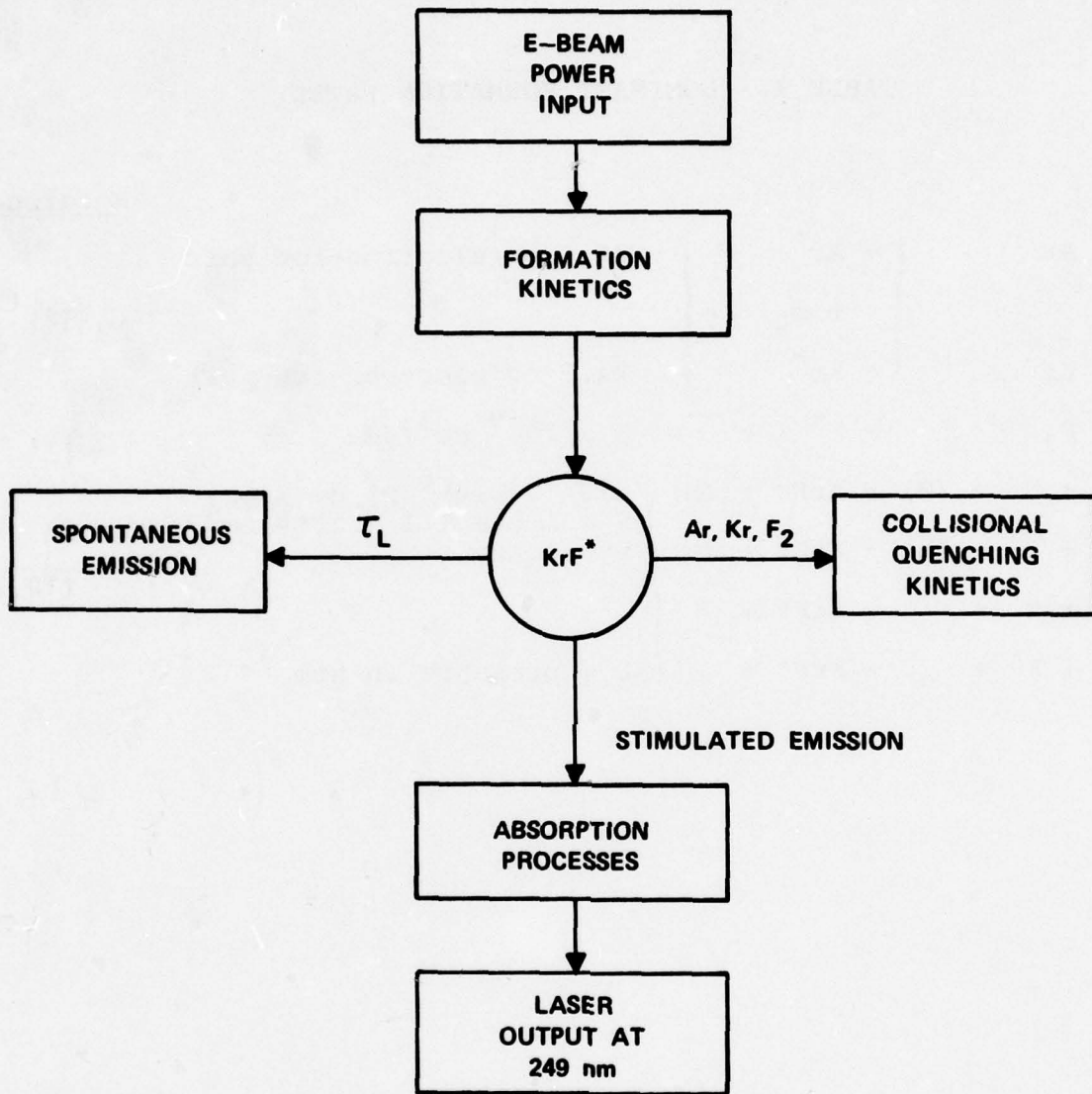
Figure 14 shows a block diagram which summarizes the important processes included in the computer code. The e-beam energy results in the formation of electron and rare gas ion pairs. The secondary electrons are rapidly lost via dissociative attachment with the halogen donor to form F^- . These ionic states eventually result in the formation of KrF^* .⁽⁵⁾ The dominant formation kinetics and corresponding rates are listed in Table 1 (Refs. 8, 9, 10, and 11). Once the KrF^* is formed, it

(8) Jesse, W.P. and Sadauskis, J., Phys. Rev. 90, 1120L (1953).

(9) Chen, Hao-Lin, Center, R.E., Trainor, D.W. and Fyfe, W.I., J. Appl. Phys. 48, 2297 (1977).

(10) Jacob, J.H., Rokni, M., Mangano, J.A. and Brochu, R., Appl. Phys. Lett. 32, 109 (1978).

(11) Flannery, M.R. and Yang, T.P., Appl. Phys. Lett. 32, 327 (1978); See also Appl. Phys. Lett. 32, 356 (1978).



H4999

Figure 14. Processes Included in the Model

TABLE 1. DOMINANT FORMATION RATES

| | | | <u>Reference</u> |
|--------------------|---------------------------|--|---|
| e^+ $e +$ | Ar Kr | $\left. \begin{array}{l} \rightarrow Ar^+ \\ + e_s + e \\ \rightarrow Kr^+ \end{array} \right\}$ | 26.4 eV/electron-ion pair 24.1 eV/electron-ion pair (8) |
| $e + F_2$ | $\rightarrow F^- + F$ | $\approx 3 \times 10^{-9} \text{ cm}^3/\text{sec}$ | (9) |
| $Ar^+ + F^- + (M)$ | $\rightarrow ArF^* + (M)$ | $(10^{-7} + 10^{-6} P) \text{ cm}^3/\text{sec};$ | (10,11) |
| $Kr^+ + F^- + (M)$ | $\rightarrow KrF^* + (M)$ | $P < 1 \text{ atm } 1.1 \times 10^{-6} \text{ cm}^3/\text{sec}$ | |
| $Ar_2^+ + F^- +$ | $\rightarrow ArF^* +$ | $P > 1 \text{ atm}$ | |
| $Kr_2^+ + F^- +$ | $\rightarrow KrF^* +$ | $P = \text{pressure in atm}$ | |

can radiatively decay, be quenched by the rare gases or halogen donor or be stimulated by the cavity flux. The rate constants for the dominant formation and quenching processes have been measured and checked by comparing the measured KrF^* fluorescence efficiency calculated using these rates for various Ar/Kr/F_2 mixtures. The dominant quenching reactions and rate constants used in the code are given in Table 2 (Refs. 5 and 12). Inclusion of these processes also enables the code to predict the number densities of species which absorb at the laser wavelength. The calculated medium absorption has been compared with measured values for various mixtures and e-beam excitation levels.⁽⁷⁾

The three important absorbing species are F_2 , F^- and Kr_2F^* . The absorption cross sections of these species^(13,14,15) are listed in Table 3. What remains to be verified is the ability of the code to predict power extraction in the presence of intrinsic medium absorption and overall laser performance for various levels of e-beam excitation and laser gas mixtures. Here this ability is checked with experiment. This comparison provides a verification of the validity of the power extraction model as well as an independent check of the various kinetics leading to laser medium gain and absorption.

-
- (12) Other scientists have investigated the quenching of KrF^* and obtained rates similar to those used in this article see for example J.G. Eden, R.W. Wayant, S.K. Searles and R. Burnham, *Appl. Phys. Lett.* 32, 733 (1978); G.P. Owgley and W.M. Hughes, *Appl. Phys. Lett.* 32, 627 (1978).
- (13) Mangano, J.A., Jacob, J.H., Rokni, M. and Hawryluk, A., *Appl. Phys. Lett.* 31, 26 (1977).
- (14) Steunenbergh, R.K. and Vogel, R.C., *J. Amer. Chem. Soc.* 78, 901 (1956).
- (15) Mandl, A., *Phys. Rev.* A3, 251 (1970).

TABLE 2. DOMINANT QUENCHING RATES

| | | | <u>Reference</u> |
|--|-------------------|-------------------------------------|---|
| $\text{KrF}^* + \text{F}_2$ | \longrightarrow | Products | $7.8 \times 10^{-10} \text{ cm}^3/\text{sec}^{-1}$ |
| $\text{KrF}^* + 2\text{Kr}$ | \longrightarrow | $\text{Kr}_2\text{F}^* + \text{Kr}$ | $6.7 \times 10^{-31} \text{ cm}^6/\text{sec}^{-1}$ |
| $\text{KrF}^* + \text{Kr} + \text{Ar}$ | \longrightarrow | $\text{Kr}_2\text{F}^* + \text{Ar}$ | $6.5 \times 10^{-31} \text{ cm}^6/\text{sec}^{-1}$ (12) |
| $\text{KrF}^* + 2\text{Ar}$ | \longrightarrow | Products | $7 \times 10^{-32} \text{ cm}^6/\text{sec}^{-1}$ |

TABLE 3. DOMINANT ABSORBING SPECIES

| <u>Species</u> | <u>Cross Section (cm²)</u> | <u>References</u> |
|-------------------|---|-------------------|
| F ₂ | 1.3 x 10 ⁻²⁰ | (13) |
| F ⁻ | 5.6 x 10 ⁻¹⁸ | (14) |
| Kr ₂ F | 1.6 x 10 ⁻¹⁸ | (15) |

B. POWER EXTRACTION

The rate of change of the cavity flux is given by

$$\frac{\partial \phi_{\pm}}{\partial t} \pm c \frac{\partial \phi_{\pm}}{\partial x} = \left(\frac{g_0 - \alpha_0}{1 + (\phi_+ + \phi_-)/\phi_s} - \alpha \right) \phi_s \quad (4)$$

where ϕ_+ (ϕ_-) is the cavity flux propagating in the positive (negative) x direction, ϕ_s is the saturation flux, g_0 is the small signal gain, α_0 and α are the saturable and nonsaturable absorption coefficients of the medium. Absorption by F_2 , F_2^- , Kr_2^+ and Ar_2^+ is nonsaturable, while the absorption by Kr_2F^* is saturable with the same saturation flux as the lasing transition, since KrF^* is the precursor of the Kr_2F^* .⁽⁵⁾ Equation (4) may be simplified by integrating over x. The temporal variation of the laser cavity flux is then determined by the following differential equation

$$\frac{d\langle \phi_c \rangle}{dt} = c \left(\frac{g_0 - \alpha_0}{1 + \langle \phi_c \rangle / \phi_s} - g_c - \alpha \right) \langle \phi_c \rangle \quad (5)$$

where $\langle \phi_c \rangle$ is the spatially averaged cavity flux, g_c the cavity loss. In writing Eq. (5) we have assumed that (1) the variations of gain and absorption along the cavity are small⁽¹⁶⁾ and (2) the

(16) The condition on the small variation of gain and absorption with x may be written explicitly as

$$\left\{ \left\langle \frac{\phi_c / \phi_s}{1 + \phi_c / \phi_s} \right\rangle - \frac{\langle \phi_c / \phi_s \rangle}{1 + \langle \phi_c / \phi_s \rangle} \right\} / \left\langle \frac{\phi_c / \phi_s}{1 + \phi_c / \phi_s} \right\rangle \ll 1$$

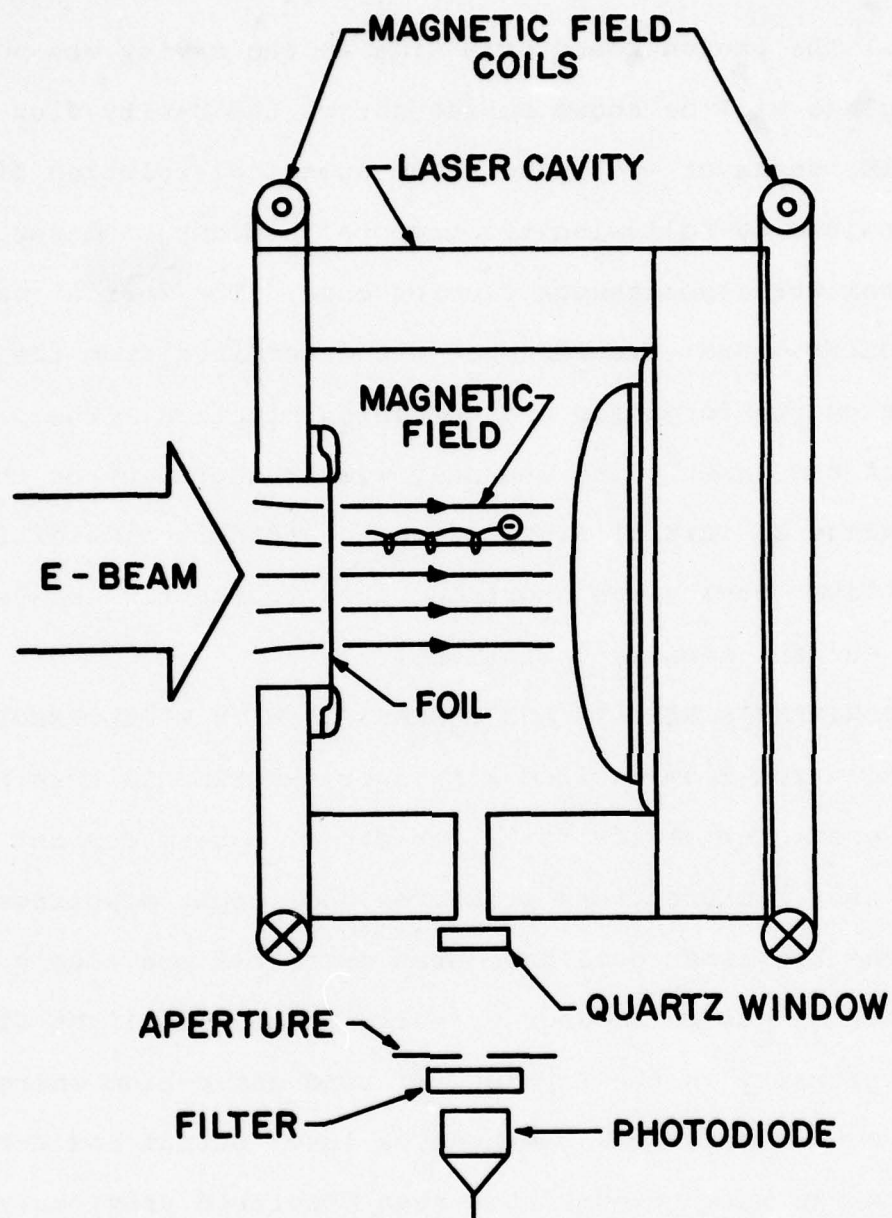
where $\langle F \rangle = 1/2 \int F(x) dx$. For the example discussed subsequently this ratio < 0.1 .

temporal variation of ϕ_c is small during one round trip in the cavity. The photon round trip time in the cavity was ~ 10 nsec, whereas, as will be shown subsequently, the cavity flux varied on a time scale of ~ 50 nsec. The numerical solution of Eq. (4) was obtained by following the temporal buildup of laser cavity flux from KrF* spontaneous fluorescence. The initial value of the isotropic KrF* fluorescence was determined from the code describing the formation and quenching kinetics. The predicted shape of the laser pulse was only weakly dependent on the calculated value of initial flux, since the transit time of the flux in the laser cavity was short compared to the time scale of the e-beam current density variations.

C. EXPERIMENTAL RESULTS AND COMPARISON WITH MODEL PREDICTIONS

Electron beam excited KrF laser experiments were performed on the one-meter device for a variety of e-beam current densities, laser mixtures, gas pressures and output couplings. The e-gun and the laser cell have been described previously.⁽¹⁷⁾ The laser output pulse energy, pulse shape, sidelight fluorescence intensity in the KrF*(B \rightarrow X) band and e-beam energy deposition were measured. Methods of laser output and e-beam input energy measurements have been described previously.⁽¹⁷⁾ The experimental arrangement used to monitor sidelight is shown schematically in Figure 15.

(17) Mangano, J.A., et al., "One-Meter KrF Laser System," Semi-Annual Report, August 21, 1976 to Feb. 22, 1977.



H4997

Figure 15. Sidelight Measurement Geometry

Figure 16 shows the comparison of the code predictions and experimental observations for a typical case. The laser mixture for this case contained 0.2% F₂, 4% Kr and 95.8% Ar at a total mixture pressure of 1.5 atm. The optical cavity output coupling was 0.66. The peak e-beam current density after attenuation by the anode screen and foil support structure was 11.5 A/cm². The e-beam pulse shape is shown in Figure 17. The top trace in Figure 16 is the KrF* sidelight pulse shape that was monitored in the absence of laser flux by an S5 photodiode. A narrow band filter ($\Delta\lambda = 70 \text{ \AA}$ FWHM) centered at 249 nm was placed in front of the photodiode. For comparison, the sidelight pulse shape predicted by our numerical code is also shown. The predicted curve was normalized to the experimental curve at the peak value. The center traces are a comparison of the sidelight under laser conditions.

The bottom traces in Figure 16 show the predicted and experimental laser pulse shapes. Experimentally, the laser energy was measured using a Scientec calorimeter and the pulse shape was monitored by a photodiode. The laser power coupled out was computed by ensuring that the integrated power was just the measured output energy. The area of the laser beam was determined from burn pattern measurements so that the output flux could be computed. Notice that the predicted pulse turns on about 40 nsec earlier than the experimental pulse. In part this is because of the assumptions made in writing Eq. (4). As the laser flux increases, the sidelight is depressed. This depression, caused by

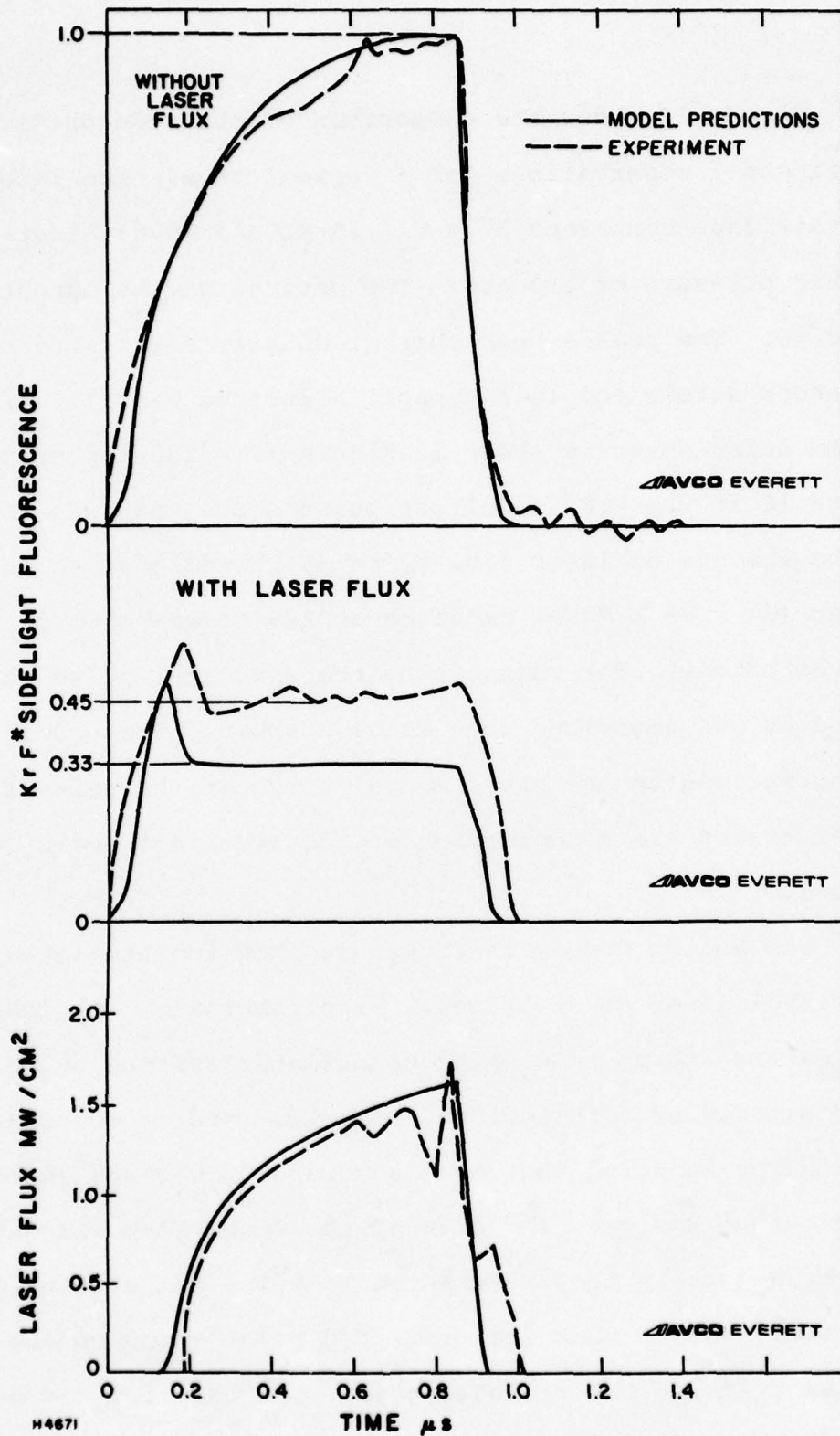
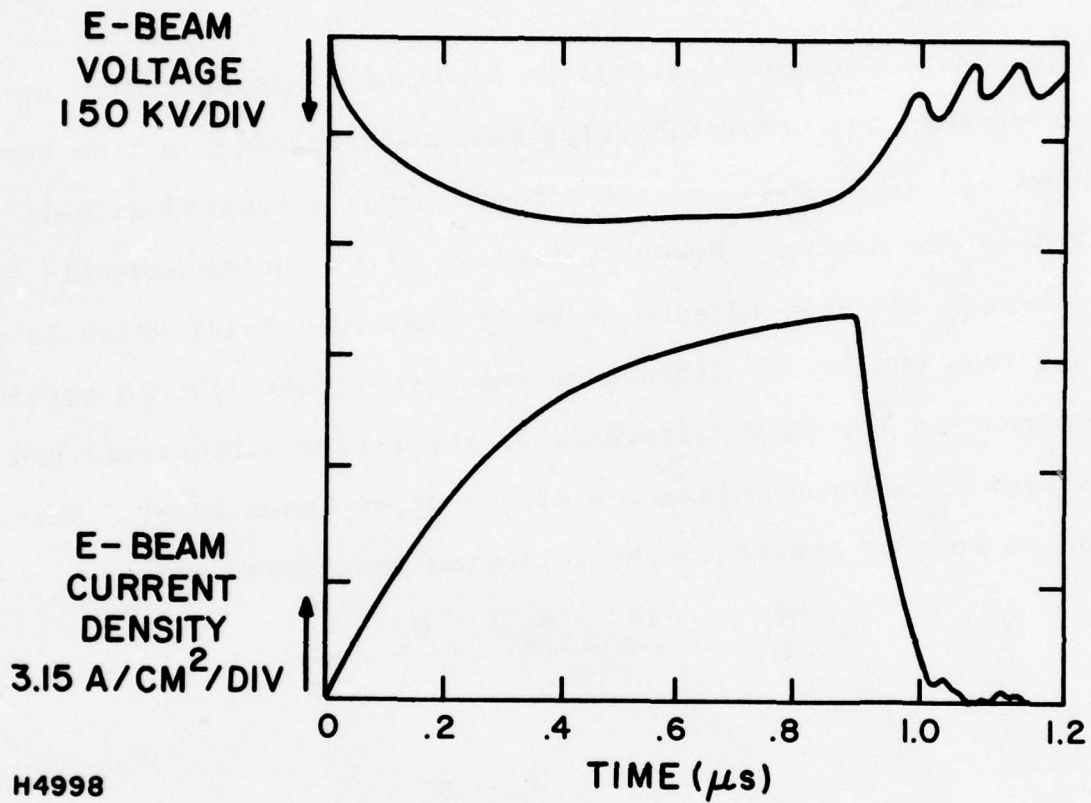


Figure 16. Comparison of Measured and Calculated Pulse Shapes



H4998

Figure 17. E-Beam Current Pulseshape

the laser cavity flux, is smaller than predicted. The experimental value is 0.45 compared to the theoretical value of 0.33.

D. DISCUSSION

The experimental sidelight amplitude is expected to be larger than the predicted value because fluorescence from the upper and lower edges of the e-beam is not saturated as well as that in the center. However, because of the guide magnetic field, we expect the edge effects to be of the order 5-10% which is much less than the 30-35% difference seen experimentally. A possible explanation for this difference is the finite vibrational and perhaps rotational relaxation of the upper laser level. This can be seen by analyzing the following rate equations:

$$\frac{dN_o}{dt} = - \frac{(N_o - N_{oe})}{\tau_v} - \frac{N_o}{\tau} - \frac{N_o}{\tau_s} \quad (6)$$

and

$$\frac{dN}{dt} = R - \frac{N}{\tau} - \frac{N_o}{\tau_s} \quad (7)$$

where N_o is the population of the zeroth level; N_{oe} is the equilibrium population of the zeroth level, $N_{oe} = \theta_o N$. θ_o is the partition function and $N = \sum_v N_v$, τ is the lifetime of the upper level, τ_s is the stimulated lifetime of the upper level, R is the pumping rate and τ_v is the vibrational relaxation rate.

Equations (6) and (7) can be solved under steady state conditions to give:

$$N/N^o = \frac{\{1 + (\phi/\phi_s) \frac{1}{\beta}\}}{(1 + \phi/\phi_s)} \quad (8)$$

where ϕ_s is the saturation flux defined previously, N^0 is the upper state population density when $\phi = 0$ and

$$\beta = 1 + \theta_0 \tau / \tau_v \quad (9)$$

Note that for $\tau_v \rightarrow 0$ $\beta \rightarrow \infty$ and the depression of the sidelight will be $(1 + \phi/\phi_s)^{-1}$. In our model we have assumed $\tau_v = 0$. To explain the 25-35% difference in the depression we require that

$$\frac{\phi}{\phi_s} \frac{1}{\beta} \approx 0.25-0.35 \text{ or } \beta \approx 8.5 \quad (10)$$

The vibrational spacing of KrF* is estimated⁽¹⁸⁾ to be 610 cm^{-1} . Hence, at room temperature $\theta_0 \sim 0.76$ if the upper level is fully relaxed. Using the value of β given by Eq. (10) the ratio $\tau/\tau_v \approx 10$. The KrF* lifetime in the laser mixture is ~ 2.9 nsec. Hence, we can estimate τ_v the vibrational relaxation time to be ~ 0.29 nsec. Assuming that Ar is responsible for the vibrational relaxation, this relaxation time corresponds to a two-body rate constant of $\sim 10^{-10} \text{ cm}^3/\text{sec}$ or a three-body rate constant of $2.7 \times 10^{-30} \text{ cm}^6/\text{sec}$. This finite vibrational relaxation rate will decrease the extraction efficiency by $1/\beta$ (Ref. 19) which is small and so we will ignore its effect in the subsequent discussion.

However, it should be noted that this decrease in extraction efficiency can be substantial for very high e-beam pumping

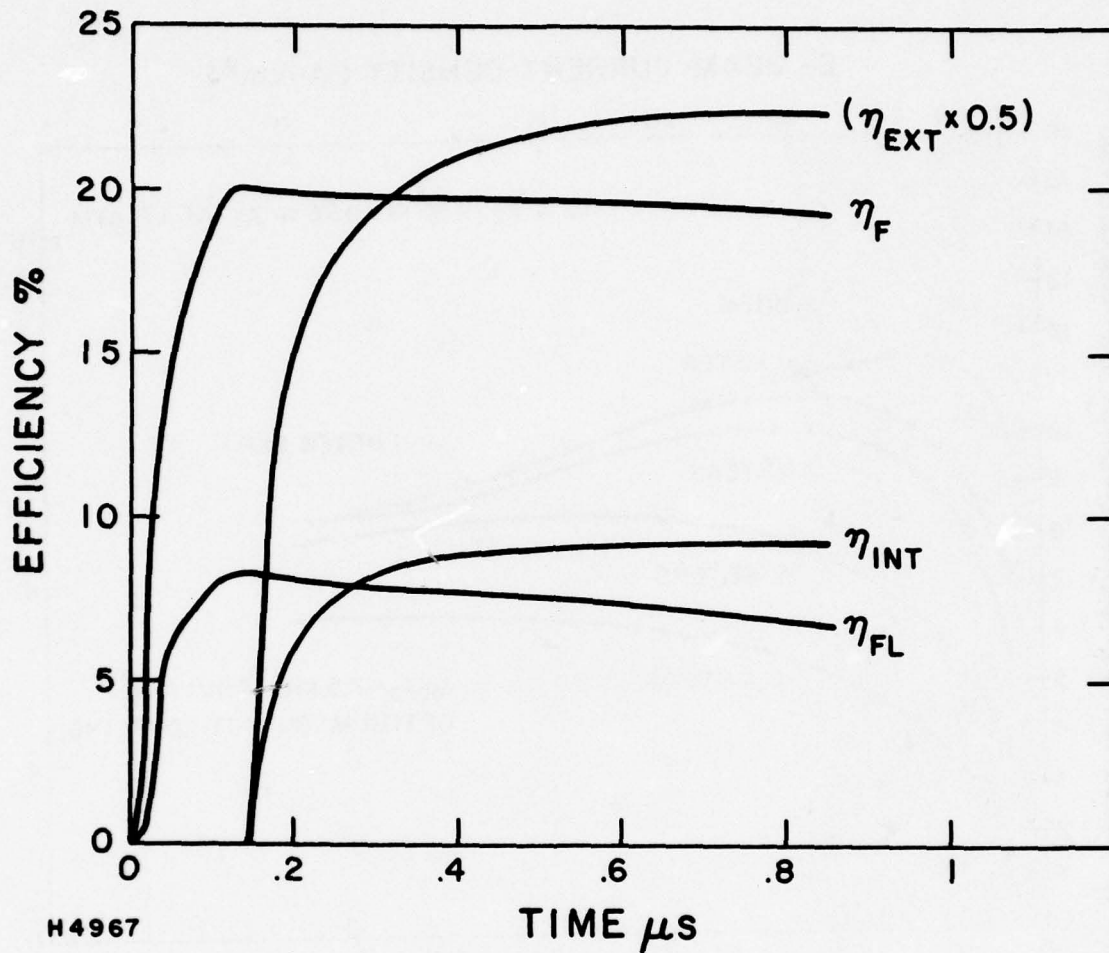
(18) Tellinghuisen, Joel, Hays, A.K., Hoffman, J.M. and Tiscione, G.C., *Journal of Chem. Phys.* 65, 4473 (1976).

(19) Rokni, M., Mangano, J.A., Jacob, J.H. and Hsia, J.C., *IEEE Journal of Quantum Electronics*, QE-14, 464 (1978).

intensities ($> 10^6$ W/cm³) where the electron density is high and electron quenching of KrF* can significantly lower τ . Also the transfer time between the B and C states of KrF will have a similar effect on the extraction efficiency. Again at low pump powers the effect is small, but it could be substantial at the higher pump power.

Figure 18 shows the predicted time dependence of the formation efficiency η_F , fluorescence efficiency η_{FL} , the laser intrinsic efficiency η_{INT} , and the laser extraction efficiency η_{EXT} . η_F is the efficiency with which KrF* is created and η_{FL} is the spontaneous power radiated divided by the e-beam power deposited. η_{EXT} is the ratio of the laser flux extracted to the number of photons available, and η_{INT} is just the product $\eta_{EXT}\eta_F$. Interestingly enough, by the end of the pulse the fluorescence efficiency is 7.5%, while the intrinsic efficiency is almost 9%. The reason that $\eta_{INT} > \eta_{FL}$ is that under lasing conditions the cavity flux is large enough to stimulate the KrF* before it can radiatively decay or be quenched by F₂ and the rare gases. Finally, η_{EXT} and η_{INT} are zero until the laser turns on, which is to be expected.

We have used our code to predict the laser output for a variety of pumping conditions. These predictions are shown in Figure 19 which is a plot of the intrinsic efficiency as a function of e-beam current density. In plotting these curves we have kept $J_{eb}\tau_p$ constant at 7.5×10^{-6} coulombs/cm², i.e., the



H4967

Figure 18. Predicted Formation Efficiency η_F , Fluorescence Efficiency η_{FL} , Intrinsic Laser Efficiency η_{INT} and Extraction Efficiency Next

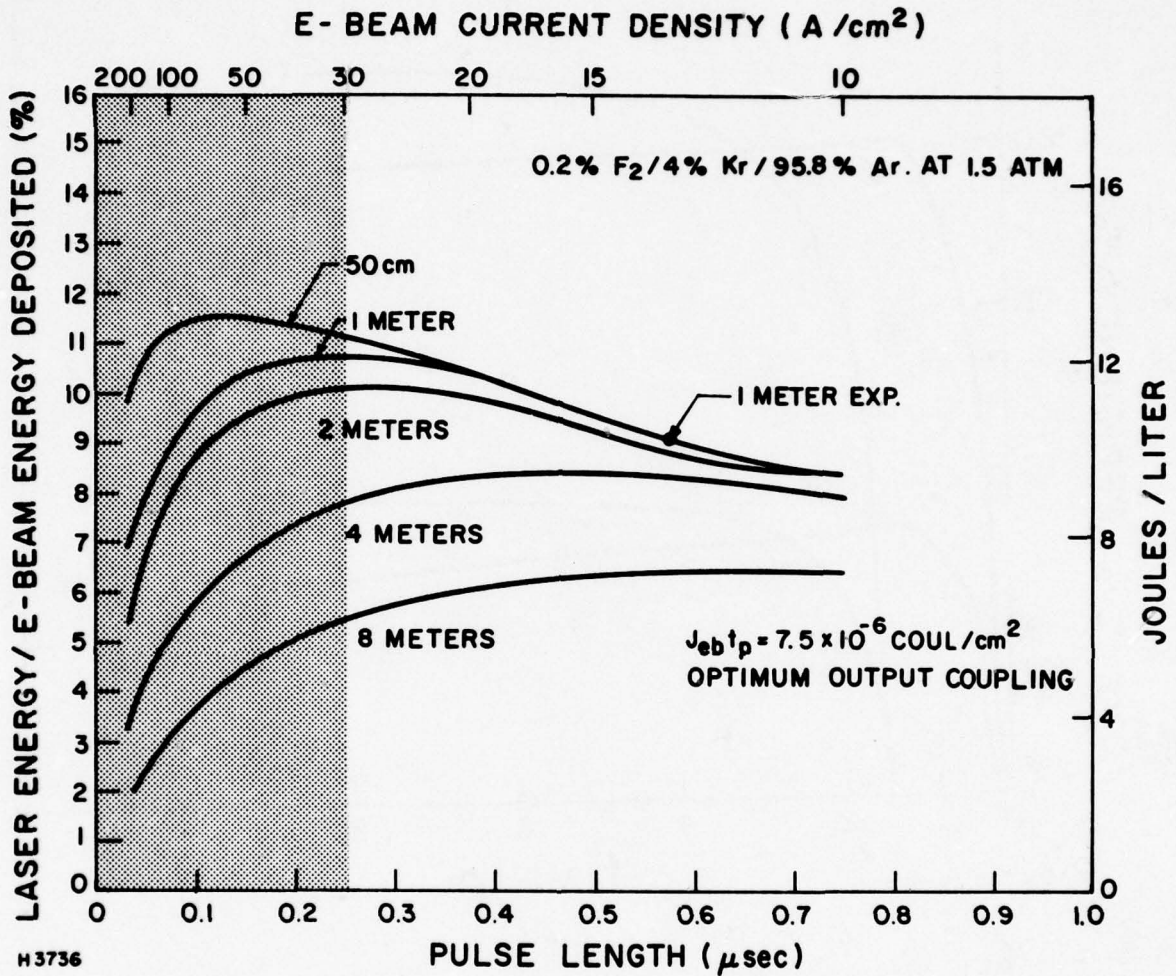


Figure 19. Predicted Laser Intrinsic Efficiency Scaling Characteristics

pump power into the laser mixture was held constant. For this pump power half the F_2 is burnt by the end of the pulse.

Notice that for a given laser length of < 2 m the laser efficiency first rises as the e-beam current density increases. This increase is because the absorbing species F^- increases only as the square root of the pump power whereas the gain increases linearly. However, the curves reach a peak and then the efficiency decreases as the pump power is increased further. The reason for this decrease is that at the higher current densities the secondary electron density increases. These secondary electrons can quench the KrF^* . In the model we have assumed a quenching rate constant of $2 \times 10^{-7} \text{ cm}^3/\text{sec}$.⁽²⁰⁾ The electron quenching of KrF^* has yet to be determined. It is partly for this reason that we have shaded the region in Figure 19 corresponding to current densities $> 30 \text{ A/cm}^2$. The efficiency for longer laser lengths also decrease. This decrease is because the product of the absorption and the laser length is greater than unity.⁽¹⁹⁾

For the present laser device the highest output energy and the highest intrinsic efficiency were observed with a laser filling pressure of 1.7 atm (0.2% F_2 /4% Kr/95.8% Ar), an average transmitted current of 11.5 A/cm^2 (13.5 A/cm^2 peak) and an optical cavity output coupling of 0.71. Under these conditions a

(20) Trainor, D.W., Rokni, M. and Jacob, J.H., 31st Gaseous Electronic Conference, Buffalo, Oct. (1978). In our model we have also assumed that the precursor for KrF^* such as ArF^* can be quenched by electrons. The rate constant used for this process is $\sim 2 \times 10^{-7} \text{ cm}^3/\text{sec}$.

total output energy of 102 J was obtained with an active laser volume of 8.5 l (12 J/l) and the intrinsic efficiency was 9%. For these conditions the code predicted an intrinsic efficiency of 9.3% and an energy extraction density of 12.5 J/l.

In conclusion, we have shown that a comprehensive computer code has been developed which can predict all the important characteristics of e-beam pumped KrF lasers for e-beam current densities $< 30 \text{ A/cm}^2$. The predictive capabilities of the code have been verified by detailed comparisons with experiment. The code should prove valuable in achieving optimal laser design as well as projecting the ultimate energy scalability of these lasers. For current densities $> 30 \text{ A/cm}^2$ the electron quenching of KrF* and other excited species could become important.

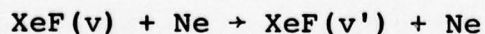
V. THEORETICAL RATE CONSTANT CALCULATIONS

In the previous reporting period we demonstrated an intrinsic XeF laser efficiency of 2.6%. Since the lower laser state of XeF is bound by $\sim 1200 \text{ cm}^{-1}$, a possible explanation for the low efficiency is bottlenecking in the lower state. Estimates based on sidelight experiments indicated that the laser efficiency was lowered by as much as a factor of two by the presence of this bottlenecking. To adequately model the laser performance one needs the rate constants for the lower level deactivation and their temperature dependences. Also, since lasing can occur in a number of $v' \rightarrow v''$ transitions, one also needs the deactivation rate constants for various specific v'' levels.

During this reporting period, a portion of the One-Meter Program was, therefore, devoted to the calculation of rate constants for the reactions:



and



These rate constants can then be incorporated into the ground state master equation, from which the time evolution of the populations of the various vibrational levels, and, hence, the deactivation lifetimes can be obtained.

To calculate these rate constants a combination of phase space theory⁽²¹⁾ and Monte Carlo trajectory calculations⁽²²⁾ was used. This is a well developed technique which has been used for a variety of three-body systems.⁽²³⁾ In the following section a description of this technique is first presented and then the results obtained to date are presented.

An effort was also undertaken to theoretically calculate the temperature dependence of recombination rate constant for



These reactions have been shown to be dominant quenching processes in KrF lasers, which limit laser efficiency at high pressures. Since the rate constants for these reactions are expected to decrease at elevated temperatures, laser performance and pressure scaling characteristics are expected to improve with increasing temperature. Knowledge of the temperature dependence of these rate constants will allow modeling of laser performance vs temperatures.

In part B of this section we briefly outline the theory and summarize the results obtained.

A. CALCULATION OF XeF GROUND STATE DISSOCIATIVE RATE CONSTANTS

A system of n particles can be described by a point in a $6n$ dimensional phase space whose coordinates are the conjugate

(21) Keck, J.C., Adv. Chem. Phys. 13, 85 (1967).

(22) Bunker, D.L., Methods Comput. Phys. 10, 287 (1971).

(23) Shui, V.H., J. Chem. Phys. 58, 4868 (1973).

momentum and position vectors (\vec{p} and \vec{q}) of the particles. The time evolution of any configuration of these n particles can be determined by following the representative point through phase space. Since phase space contains all possible interaction configurations of the n particles, it is possible to define a surface which divides space into two regions, one of which contains "reactants" and the other "products." The rate of a reaction can then be defined as the one-way flow of points across the dividing surface.

$$R_s = \int_S p \rho (\vec{v} \cdot \vec{n}) dS \quad (11)$$

where R_s is the rate of reaction, $\rho(\vec{p} \cdot \vec{q})$ is the density of points, \vec{n} is the unit vector outward normal to dS and \vec{v} is the generalized velocity in phase space. The components of \vec{v} may be obtained from the equations

$$\dot{q}_i = \frac{\partial H}{\partial p_i} \text{ and } \dot{p}_i = - \frac{\partial H_i}{\partial q(i)} \quad (12)$$

where $H(\vec{p}, \vec{q})$ is the Hamiltonian of the system. In Eq. (11), p is a reaction probability which corrects for multiple passes of the same point over the surface S . The rate coefficient, which is independent of concentration, can then be defined by

$$k_s = R_s / \prod [M_i], \quad (13)$$

where $[M_i]$ is the concentration of species i in the initial state.

Due to the presence of the unknown function p in the integrand of Eq. (11), the expression for R_s cannot be evaluated

analytically. Monte Carlo methods are, therefore, used. Monte Carlo techniques allow one to randomly pick initial conditions for the system under investigation and follow the time behavior of the particles using the equations of motion, defined in Eq. (12). An estimate of the fraction of trajectories which react, and remain reacted, can thus be obtained and this information used to determine p . A more detailed description of both the Monte Carlo techniques used in this study and phase space theory can be found in Ref. 23.

In order to solve the equations of motion used in the Monte Carlo procedure, it is necessary to know the manner in which the various particles interact. Ideally, this should be determined from a three-body potential energy surface; however, for the Xe-F-Ne system, no such surface has been calculated. To avoid this problem we have made the assumption that a three-body interaction can be approximated by the sum of the individual two-body potentials.

Information on the ground state potential of XeF is available from several sources. Smith and Kobrinsky⁽³⁾ used absorption spectroscopy to determine the ground state well depth and spectroscopic constants. Tellinghuisen, et al.,⁽⁴⁾ obtained emission spectra for the $B \rightarrow X$ and $D \rightarrow X$ transitions in XeF and applied RKR methods to this data to obtain the ground state potential curve. In addition, crossed molecular beam experiments on the

Xe(¹s) + F(²P) system have been performed by Becker, et. al. (25) Agreement between Refs. 4 and 24 is excellent.

For ease of computation, we have assumed that the ground state of XeF can be described with sufficient accuracy by a Leonard-Jones potential. A Leonard-Jones potential correctly models the behavior at large internuclear separations, but is too attractive in the region near the equilibrium separation. To determine the magnitude of the error that this assumption introduces into our results, we also ran test cases with a 12-8 potential, which more accurately models behavior near the equilibrium internuclear distance, but is too repulsive at large separations.

It was assumed that the F-Ne interaction could be approximated by that of Ne-Ne. Again, a Leonard-Jones potential, using the Ne₂ ground state spectroscopic parameters of Tanaka and Yoshino, (25) was assumed. The binding energy and equilibrium internuclear distance of Xe-Ne were estimated by the arithmetic mean of the Xe₂ (26) and Ne₂ (25) internuclear separations and the geometric mean of the binding energies. To test the sensitivity of our results to these well depths and shapes, test cases were

(24) Becker, C.H., Casavecchio, P. and Lee, Y.T., J. Chem. Phys. 69, 2377 (1978).

(25) Tanaka, Y., and Yoshino, K., J. Chem. Phys. 57, 2964 (1972).

(26) Docken, K.K. and Schafer, T.P., J. Mol. Spect. 46, 454 (1973).

run using strictly repulsive potentials of the form, $V = A_i \exp(-r/L_i)$ for both F-Ne and Xe-Ne. The parameters A_i and L_i were obtained from papers by Abrahamson⁽²⁷⁾ and Mason and Vanderslice.⁽²⁸⁾

Calculations were performed for the first six vibrational levels of XeF. Both dissociative and $V \rightarrow T, R$ rate constants were obtained. For the results reported here, it was assumed that the rotational states of any given vibrational level were in Boltzmann equilibrium up to the dissociation limit of the molecule. The validity of this assumption will be investigated in detail at a later date.

The dissociative rate constants are shown in Figure 20. Changing the forms of the various interaction potentials, made no appreciable difference to either the dissociative or $V \rightarrow T, R$ constants. The error bars indicate the uncertainty in our results caused by limited statistics. For initial vibrational quantum numbers of 0 and 1, the number of reactive trajectories, which are used to determine p in Eq. (11), is small and can induce noticeable error in the calculations. This effect becomes even more important for the $V \rightarrow T, R$ rate constants. In order to minimize the effect of statistical fluctuations, the calculated rate constants were fit to analytic expressions which have been shown to accurately model a wide variety of systems.⁽²³⁾ The dissociative rate constants were fit to the function

(27) Abrahamson, A.A., Phys. Rev. 178, 76 (1969).

(28) Mason, E.A., and Vanderslice, J.T., J. Chem. Phys. 28, 432 (1958).

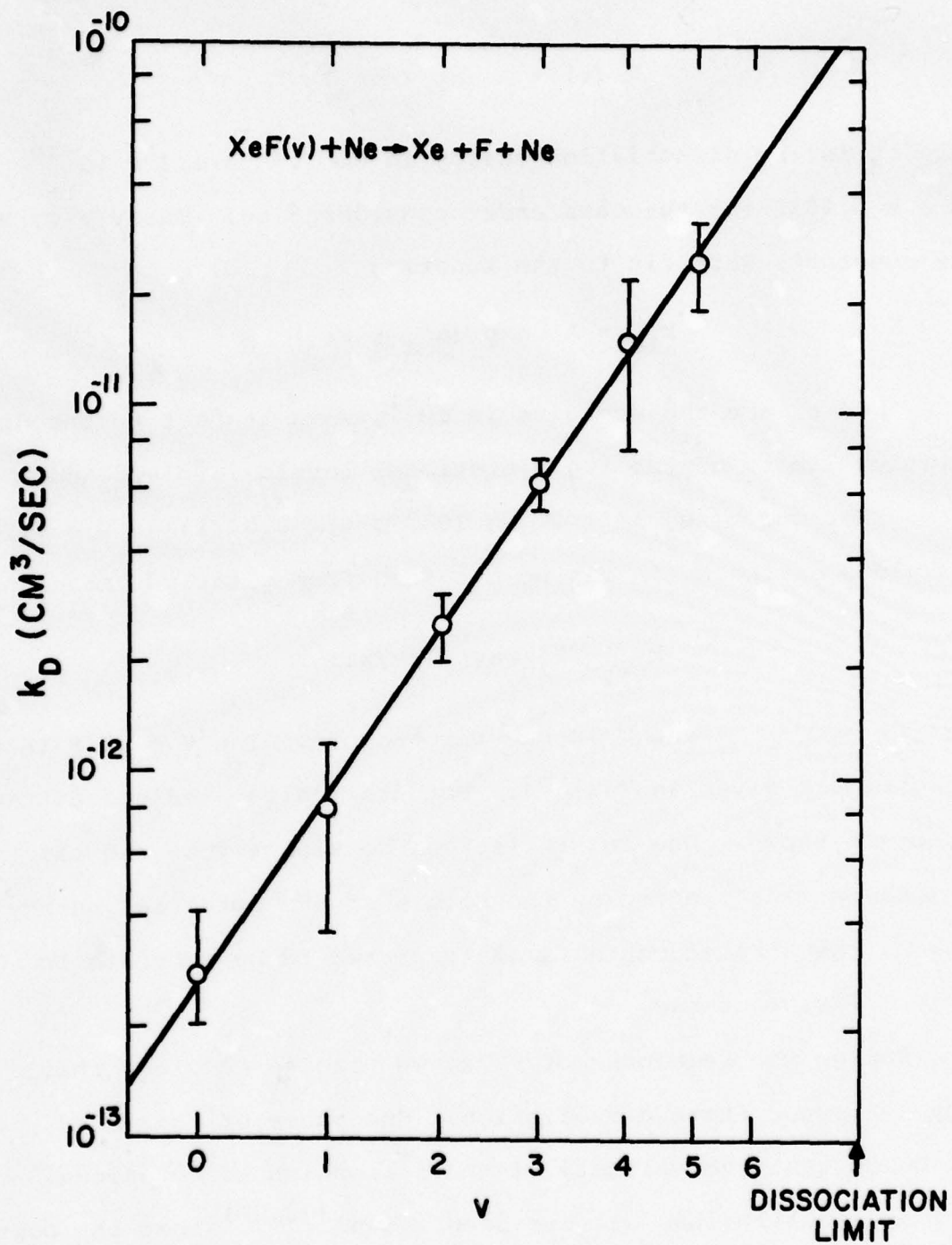


Figure 20. Calculated Dissociative Rate Constants for Various XeF Vibrational Levels

$$k_D(v) = A \exp(-\alpha \epsilon_d)$$

where ϵ_d is the dissociation energy in cm^{-1} , $A = 1.3 \times 10^{-10}$ and $\alpha = 0.0058$ for the case under consideration. The $V \rightarrow T$, R rate constants were fit to the function

$$k_{\ell u} = A' \exp(\alpha \epsilon_\ell - \beta \epsilon_u)$$

and ϵ_ℓ and ϵ_u are the energies in cm^{-1} , with respect to the dissociation limit, of the two vibrational levels involved and $\ell < u$. For our case, $A' = 2.7 \times 10^{-11}$, $\alpha = 0.0121$ and $\beta = 0.0091$. The values of the $k_{u\ell}$'s can be obtained from detailed balancing.

$$k_{u\ell} = k_{\ell u} \exp(\Delta\epsilon/kT),$$

where $\Delta\epsilon = \epsilon_u - \epsilon_\ell$ and T is the temperature. The $V \rightarrow T$, R rate constants are given in Table 4. Both the calculated and fitted values are shown. Due to statistical considerations and the assumptions made concerning the nature of the potential energy surface, these rate constants are expected to be accurate to within a factor of two.

During the remainder of FY78, we plan to complete this study of ground state dissociation. One phase of this study will be to test the validity of the assumption of rotational Boltzmann equilibrium. It has been shown,^(23,29) that the population of states close to the dissociation limit is generally less than would be predicted for Boltzmann equilibrium. This

(29) Keck, J.C., and Carrier, G.F., J. Chem. Phys. 43, 2284 (1965).

TABLE 4. $V \rightarrow T$, R RATE CONSTANTS (a) FOR $XeF(v) + Ne \rightarrow XeF(v') + Ne$

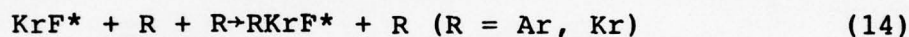
| v/v' | 0 | 1 | 2 | 3 | 4 | 5 | 6 |
|--------|-------------------------------|-------------------------------|-------------------------------|-------------------------------|-------------------------------|-------------------------------|-------|
| 0 | ----- 1.9E-12 (2.5E-12) | 3.4E-13 (9.0E-13) | 8.1E-14 (1.6E-13) | 2.3E-14 (3.8E-14) | 8.1E-15 (2.9E-15) | 3.4E-15 (3.3E-15) | |
| 1 | 5.0E-12 (8.5E-12) | ----- 3.8E-12 (1.0E-11) | 9.0E-12 (2.0E-12) | 2.6E-13 (5.8E-13) | 9.1E-14 (6.5E-14) | 3.8E-14 (8.4E-14) | |
| 2 | 2.1E-12 (2.5E-12) | 9.0E-12 (2.1E-11) | ----- 7.8E-12 (1.5E-11) | 2.3E-12 (1.0E-12) | 7.9E-13 (5.1E-14) | 3.3E-13 (9.1E-14) | |
| 3 | 1.1E-12 (1.1E-12) | 4.7E-12 (4.4E-12) | 1.7E-11 (1.1E-11) | ----- 1.5E-11 (1.8E-11) | 5.3E-12 (2.4E-12) | 2.3E-12 (1.95E-12) | |
| 4 | 6.3E-13 (7.4E-13) | 2.7E-12 (1.1E-12) | 9.6E-12 (2.9E-12) | 3.0E-11 (3.0E-11) | ----- 2.8E-11 (3.0E-11) | 1.2E-11 (5.4E-12) | |
| 5 | 3.9E-13 (7.4E-13) | 1.6E-12 (2.0E-12) | 5.9E-12 (3.8E-12) | 1.9E-11 (3.7E-12) | 5.0E-11 (1.4E-11) | ----- 4.9E-11 (6.1E-11) | |
| 6 | 2.6E-13 | 1.1E-12 | 4.0E-12 | 1.2E-11 | 3.4E-11 | 7.8E-11 | ----- |

(a) Rate constants are in units of cm^3/sec . $1.9\text{E-12} = 1.9 \times 10^{-12}$, etc. Values in parentheses are calculated; others are from analytic fit.

means that the dissociative rate constants reported here weigh the contributions from high lying rotational levels too heavily and, as a result, will be too large. We will determine the effect of the rotational distribution on the rate constants during the second half of this program. In addition, a computer code will be written to solve the master equation of the ground state which should enable us to estimate the lower lasing level deactivation lifetime.

B. TEMPERATURE DEPENDENCE OF KrF* RECOMBINATION RATE CONSTANTS

The rate constant for reactions of the type



can be calculated using the technique of Shui.⁽³⁰⁾ The rate constant can be written as

$$k_r = k_r^B (N/N_0) (k/k_e), \quad (15)$$

where N/N_0 is a correction factor for the recrossing of the phase-space surface, k/k_e is a correction factor for the nonequilibrium internal energy distribution, and k_r^B is the barrier rate constant given by

$$k_r^B = 4\pi^2 f a^2 z_2^2 (z_2 - z_1) (8kT/\pi\mu_{XY})^{1/2} [1 - \exp(-B_m/kT)]. \quad (16)$$

Details of the method of calculation have been presented in Ref. 30 and will not be repeated here. However, for the purpose or providing a simple physical explanation for the form of Eq. (16)

(30) Shui, V.H., Appl. Phys. Lett. 31, 50 (1977).

we may point out that the factor $4\pi z_2^2(z_2 - z_1)$ is a molecular volume proportional to the number of atom pairs (X-Y) close enough to recombine, whereas the factor $\pi a^2(8kT/\pi\mu_{XY})^{1/2}$ is a rate constant proportional to the frequency at which the (X-Y) pairs are stabilized under the influence of the third body M. The quantity f is the degeneracy factor, and the additional factor $[1 - \exp(-B_m/kT)]$ simply eliminates those atom pairs which cannot form bound molecules because of their excessive orbital angular momentum.

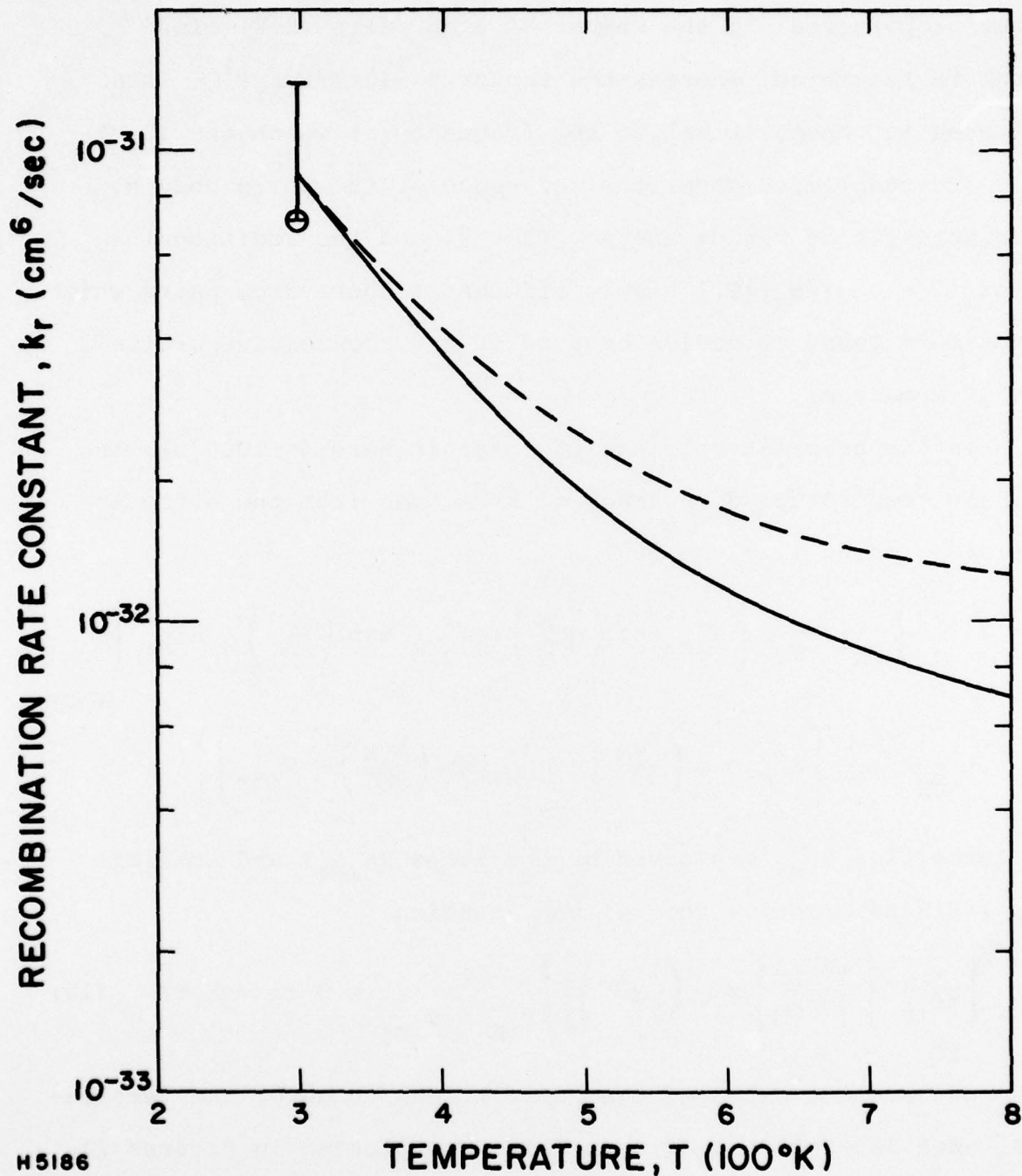
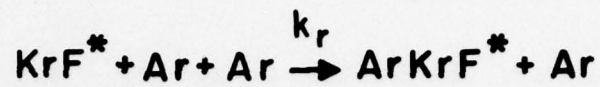
In the temperature range of interest here ($< 1000^\circ\text{K}$), the dominant temperature dependence of k_r^B comes from the effective collision radius a , given by

$$a^2 = 2^{-3/2} \left\{ \frac{m_Y}{m_X + m_Y} \left[a_{XM-}^2 \exp\left(\frac{U_{XM}}{kT}\right) + a_{XM+}^2 \exp\left(\frac{U_{XM}}{kT}\right) - a_{XM+}^2 \right] \right. \\ \left. + \frac{m_X}{m_X + m_Y} \left[a_{YM-}^2 \exp\left(\frac{U_{YM}}{kT}\right) + a_{YM+}^2 \exp\left(\frac{U_{YM}}{kT}\right) - a_{YM+}^2 \right] \right\} \quad (17)$$

The quantities $a_{iM\pm}$ are given by the large (a_{iM+}) and smaller (a_{iM-}) finite positive root of the equation

$$\left\{ \frac{d}{dr_{iM}} \left[\left| \frac{dv_{iM}}{dr_{iM}} \right| \exp\left(\frac{-v_{iM}}{kT}\right) \right] \right\}_{r_{iM} = a_{iM\pm}} = 0 \quad (i = X, Y) \quad (18)$$

We have now extended the calculations to cover the temperature range $300\text{-}800^\circ\text{K}$, and the results are plotted in Figures 21 and 22 for $R = \text{Ar}$ and $R = \text{Kr}$, respectively. In each figure the recombination rate constant is plotted vs temperature, illustrating



H5186

Figure 21. Calculated Recombination Rate Constant vs Temperature $R = \text{Ar}$

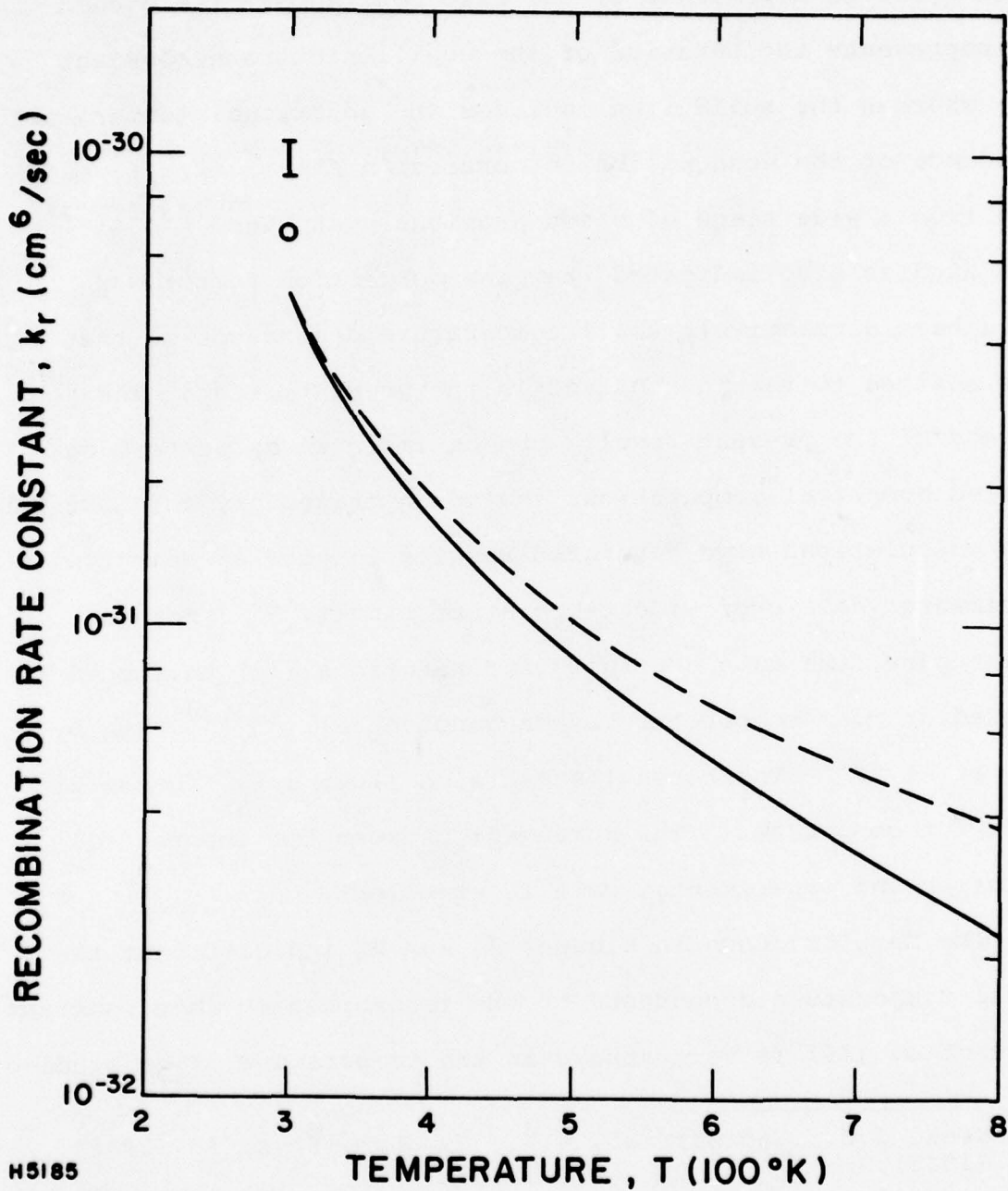
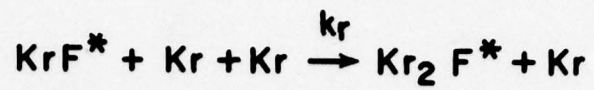


Figure 22. Calculated Recombination Rate Constant vs Temperature R = Kr

the temperature dependence of the rate constants. The dashed line represents the behavior of the equilibrium rate constant (k_r^B) whereas the solid line includes the additional temperature dependence of the nonequilibrium correction factor (k/k_e), estimated from a wide range of cases previously studied.^(23,31,32) These studies also indicated that the correction factor N/N_0 should have a relatively small temperature dependence so that it is assumed to remain constant in the present study. The accuracy of the present results can be improved by performing detailed numerical computations including trajectory calculations. These calculations have generated results in good agreement with experimental data over wide temperature ranges.⁽²³⁾ For the present case, the rate constants for reactions (14) have been measured at room temperature by Mangano, et al.,^(33,34) and by Eden, et al.⁽³⁵⁾ Their results are also plotted in Figures 21 and 22 for comparison. The agreement between the theoretical prediction and experimental data is excellent.

The results shown in Figures 21 and 22 indicate that the overall temperature dependence of the recombination rate constants for reaction (14) is very strong in the temperature range studied

-
- (31) Keck, J.C., and Carrier, G.F., J. Chem. Phys. 43, 2284 (1965).
- (32) Shui, V.H., J. Chem. Phys. 57, 1704 (1972).
- (33) Mangano, J.A., Jacob, J.H., Rokni, M., and Hawryluk, A., Appl. Phys. Lett. 31, 26 (1977).
- (34) Rokni, M., Jacob, J.H., and Mangano, J.A., Phys. Rev. A 16, 2216 (1977).
- (35) Eden, J.G., Waynant, R.W., Searles, S.K., and Burnham, R., Appl. Phys. Lett. 32, 733 (1978).

(300-800°K). For example, a change in temperature from 300°K to 600°K lowers $k_r(\text{Ar})$ by a factor of 8 and $k_r(\text{Kr})$ by a factor of 10. These theoretical predictions should be very useful in making projections for laser performance and in making plans for additional experiments.

VI. PLANS FOR NEXT PERIOD

For the next period the one-meter laser device will be used to study KrF laser performance at elevated temperatures. Theoretical calculations presented in Section V indicate that three-body quenching of KrF* by Kr and Ar should decrease dramatically with increased temperature. This decrease is expected to lead to higher small signal gain and also reduced absorption at the laser wavelength due to the formation of Kr₂F*. These effects should lead to improved laser performance, particularly at high pressure.

Also, for the next period, discharge-pumped HgCl laser experiments will be performed. Cl₂ will be used for these experiments. Discharge modeling calculations indicate high (> 80%) Hg*(³P) formation efficiency in an e-beam controlled discharge. Cl₂ is expected to react with Hg*(³P_{0,1,2}) states to form HgCl* with high efficiency. If the extraction efficiency is comparable to that found in the rare gas-halide lasers, then a HgCl intrinsic laser efficiency of 20% may be achievable. Small scale HgCl* experiments have been hampered by spontaneous heterogeneous pre-reaction problems between Hg and Cl₂. These problems are expected to be much less severe in the one-meter device because of the larger volume-to-surface ratio.

In parallel with the above, theoretical rate constant calculations for collisional deactivation of XeF ground state via vibrational excitation/de-excitation and dissociation will be continued into the next period. The results of these calculations will be incorporated into a comprehensive XeF laser model and the model predictions will be compared with experimental results.

REFERENCES

1. Hsia, J.C., Mangano, J.A., Jacob, J.H., Rokni, M., "One-Meter KrF Laser System," Semi-Annual Report, Feb. 23, 1977 to Aug. 22, 1978.
2. Mangano, J.A. and Jacob, J.H., Appl. Phys. Lett. 27, 495 (1975).
3. Smith, A.L., Kobrinsky, P.C., J. Mol. Spect. 69, 1 (1978).
4. Tellinghuisen, P.C., et al., J. Chem. Phys. 68, 5187 (1978).
5. Rokni, M., Jacob, J.H. and Mangano, J.A., Phys. Rev. A16, 2216 (1977).
6. Velazco, J.E., Kolts, J.H. and Setser, D.W., J. Chem. Phys. 65, 3468 (1976).
7. Hawryluk, A.M., Mangano, J.A. and Jacob, J.H., Appl. Phys. Lett. 31, 164 (1977).
8. Jesse, W.P. and Sadauskis, J., Phys. Rev. 90, 2230L (1953).
9. Chen, Hao-Lin, Center, R.E., Trainor, D.W. and Fyfe, W.I., J. Appl. Phys. 48, 2297 (1977).
10. Jacob, J.H., Rokni, M., Mangano, J.A. and Brochu, R., Appl. Phys. Lett. 32, 109 (1978).
11. Flannery, M.R. and Yang, T.P., Appl. Phys. Lett. 32, 327 (1978); See also Appl. Phys. Lett. 32, 356 (1978).
12. Other scientists have investigated the quenching of KrF* and obtained rates similar to those used in this article see for example J.G. Eden, R.W. Wayant, S.K. Searles and R. Burnham, Appl. Phys. Lett. 32, 733 (1978); G.P. Owgley and W.M. Hughes, Appl. Phys. Lett. 32, 627 (1978).
13. Mangano, J.A., Jacob, J.H., Rokni, M. and Hawryluk, A., Appl. Phys. Lett. 31, 26 (1977).
14. Steunenberg, R.K. and Vogel, R.C., J. Amer. Chem. Soc. 78, 901 (1956).
15. Mandl, A., Phys. Rev. A3, 251 (1970).

16. The condition on the small variation of gain and absorption with x may be written explicitly as

$$\left\{ \left\langle \frac{\phi_c/\phi_s}{1 + \phi_c/\phi_s} \right\rangle - \frac{\langle \phi_c/\phi_s \rangle}{1 + \langle \phi_c/\phi_s \rangle} \right\} / \left\langle \frac{\phi_c/\phi_s}{1 + \phi_c/\phi_s} \right\rangle \ll 1$$

where $\langle F \rangle = 1/2 \int F(x) dx$. For the example discussed subsequently this ratio < 0.1 .

17. Mangano, J.A., et al., "One-Meter KrF Laser System," Semi-Annual Report, August 21, 1976 to Feb. 22, 1977.
18. Tellinghuisen, Joel, Hays, A.K., Hoffman, J.M. and Tiscone, G.C., Journal of Chem. Phys. 65, 4473 (1976).
19. Rokni, M., Mangano, J.A., Jacob, J.H. and Hsia, J.C., IEEE Journal of Quantum Electronics, QE-14, 464 (1978).
20. Trainor, D.W., Rokni, M. and Jacob, J.H., 31st Gaseous Electronic Conference, Buffalo, Oct. (1978). In our model we have also assumed that the precursor for KrF* such as ArF* can be quenched by electrons. The rate constant used for this process is $\sim 2 \times 10^{-7}$ cm³/sec.
21. Keck, J.C., Adv. Chem. Phys. 13, 85 (1967).
22. Bunker, D.L., Methods Comput. Phys. 10, 287 (1971).
23. Shui, V.H., J. Chem. Phys. 58, 4868 (1973).
24. Becker, C.H., Casavecchio, P. and Lee, Y.T., J. Chem. Phys. 69, 2377 (1978).
25. Tanaka, Y. and Yoshino, K., J. Chem. Phys. 57, 2964 (1972).
26. Docken, K.K. and Schafer, T.P., J. Mol. Spect. 46, 454 (1973).
27. Abrahamson, A.A., Phys. Rev. 178, 76 (1969).
28. Mason, E.A. and Vanderslice, J.T., J. Chem. Phys. 28, 432 (1958).
29. Keck, J.C. and Carrier, G.F., J. Chem. Phys. 43, 2284 (1965).
30. Shui, V.H., Appl. Phys. Lett. 31, 50 (1977).
31. Keck, J.C. and Carrier, G.F., J. Chem. Phys. 43, 2284 (1965).

32. Shui, V.H., J. Chem. Phys. 57, 1704 (1972).
33. Mangano, J.A., Jacob, J.H., Rokni, M. and Hawryluk, A., Appl. Phys. Lett. 31, 26 (1977).
34. Rokni, M., Jacob, J.H. and Mangano, J.A., Phys. Rev. A16, 2216 (1977).
35. Eden, J.G., Waynant, R.W., Searles, S.K. and Burnham, R., Appl. Phys. Lett. 32, 733 (1978).

PRECEDING PAGE BLANK-NOT FILMED

DISTRIBUTION LIST

Office of Naval Research, Department of the Navy, Arlington, VA 22217 - Attn: Physics Program (3 copies)
Naval Research Laboratory, Department of the Navy, Washington, DC 20375 - Attn: Technical Library (1 copy)
Office of the Director of Defense, Research and Engineering, Information Office Library Branch, The Pentagon, Washington, DC 20301 (1 copy)
U.S. Army Research Office, Box CM, Duke Station, Durham, NC 27706 (1 copy)
Defense Documentation Center, Cameron Station, Alexandria, VA 22314 (12 copies)
Defender Information Analysis Center, Battelle Memorial Institute, 505 King Avenue, Columbus, OH 43201 (1 copy)
Commanding Officer, Office of Naval Research Branch Office, 536 South Clark Street, Chicago, IL 60615 (1 copy)
New York Area Office, Office of Naval Research, 715 Broadway (5th Floor), New York, NY 10003 - Attn: Dr. Irving Rowe (1 copy)
Air Force Office of Scientific Research, Department of the Air Force, Washington, DC 22209 (1 copy)
Office of Naval Research Branch Office, 1030 East Green Street, Pasadena, CA 91106 - Attn: Dr. Robert Behringer (1 copy)
Defense Advanced Research Projects Agency, 1400 Wilson Blvd., Arlington, VA 22209 - Attn: Strategic Technology Office (1 copy)
Office Director of Defense, Research & Engineering, The Pentagon, Washington, DC 20301 - Attn: Assistant Director (Space and Advanced Systems) (1 copy)
Office of the Assistant Secretary of Defense, System Analysis (Strategic Programs), Washington, DC 20301 - Attn: Mr. Gerald R. McNichols (1 copy)
U.S. Arms Control and Disarmament Agency, Dept. of State Bldg., Rm. 4931, Washington, DC 20451 - Attn: Dr. Charles Henkin (1 copy)
Energy Research Development Agency, Division of Military Applications, Washington, DC 20454 (1 copy)
National Aeronautics & Space Administration, Lewis Research Center, Cleveland, OH 44135 - Attn: Dr. John W. Dunning, Jr. (1 copy) (Aerospace Res. Engineer)
National Aeronautics & Space Administration, Code RR, FOB 10B, 600 Independence Ave., SW, Washington, DC 20546 (1 copy)
National Aeronautics and Space Administration, Ames Research Center, Moffett Field, CA 94035 - Attn: Dr. Kenneth W. Billman (1 copy)
Department of the Army, Office of the Chief of RD&A, Washington, DC 20310 - Attn: DARD-DD (1 copy) DAMA-WSM-T (1 copy)
Department of the Army, Office of the Deputy Chief of Staff for Operations & Plans, Washington, DC 20310 - Attn: DAMO-RQD (1 copy)
U.S. Army Missile Command, Research & Development Division, Redstone Arsenal, AL 35809 - Attn: Army High Energy Laser Programs (2 copies)
Commanding Officer, U.S. Army Mobility Equipment R&D Center, Ft. Belvoir, VA 22060 - Attn: SMEFB-MW (1 copy)
Commander, U.S. Army Armament Command, Rock Island, IL 61201 - Attn: AMSAR-RDT (1 copy)
Director, Ballistic Missile Defense Advanced Technology Center, P.O. Box 1500, Huntsville, AL 35807 - Attn: ATC-O (1 copy) ACT-T (1 copy)
Commanding General, U.S. Army Munitions Command, Dover, NH 17801 - Attn: Mr. Gilbert F. Chesnov (AMSMU-R) (1 copy)
Director, U.S. Army Ballistics Res. Lab, Aberdeen Proving Ground, MD 21005 - Attn: Dr. Robert Eichenberger (1 copy)
Commandant, U.S. Army, Air Defense School, Ft. Bliss, TX 79916 - Attn: Air Defense Agency (1 copy) ATSA-CTD-MS (1 copy)
Commanding General, U.S. Army Combat Dev. Command, Ft. Belvoir, VA 22060 - Attn: Director of Material, Missile Div. (1 copy)
Commander, U.S. Army Training & Doctrine Command, Ft. Monroe, VA 23651 - Attn: ATCD-CF (1 copy)
Commander, U.S. Army Electronics Command, Ft. Monmouth, NJ 07703 - Attn: AMSEL-CT-L, Dr. R.G. Buser (1 copy)
Commander, U.S. Army Combined Arms Combat Developments Activity, Ft. Leavenworth, KS 66027 (1 copy)
National Security Agency, Ft. Geo. G. Meade, MD 20755 - Attn: R.C. Foss A763 (1 copy)
Deputy Commandant for Combat & Training Developments, U.S. Army Ordnance Center and School, Aberdeen Proving Ground, MD 21005 Attn: ATSL-CTD-MS-R (1 copy)
Department of the Navy, Office of the Chief of Naval Operations, The Pentagon 5C739, Washington, DC 20350 - Attn: (OP 982F3) (1 copy)
Office of Naval Research Branch Office, 495 Summer Street, Boston, MA 02210 - Attn: Dr. Fred Quella (1 copy)

DISTRIBUTION LIST (Continued)

Department of the Navy, Deputy Chief of Navy Material (Dev.), Washington, DC 20360 - Attn: Mr. R. Gaylord (MAT 032B) (1 copy)

Naval Missile Center, Point Mugu, CA 93042 - Attn: Gary Gibbs (Code 5352) (1 copy)

Naval Research Laboratory, Washington, DC 20375 - Attn: Electro-Optical Technology Program Office, Code 1409 (1 copy)
Dr. P. Livingston - Code 5560 (1 copy)
Dr. A.I. Schindler - Code 6000 (1 copy)
Dr. John L. Walsh - Code 5503 (1 copy)

High Energy Laser Project Office, Department of the Navy, Naval Sea Systems Command, Washington, DC 20360 -
Attn: Capt. A. Skolnick, USN (PM 22) (1 copy)

Superintendent, Naval Postgraduate School, Monterey, CA 93940 - Attn: Library (Code 2124) (1 copy)

Navy Radiation Technology, Air Force Weapons Lab (NLO), Kirtland AFB, NM 87117 (1 copy)

Naval Surface Weapons Center, White Oak, Silver Spring, MD 20910 - Attn: Dr. Leon H. Schindel (Code 310) (1 copy)
Dr. E. Leroy Harris (Code 313) (1 copy)
Mr. K. Enkenhaus (Code 034) (1 copy)
Mr. J. Wise (Code 047) (1 copy)
Technical Library (1 copy)

U.S. Naval Weapons Center, China Lake, CA 93555 - Attn: Technical Library (1 copy)

HQ USAF (AF/RDPS), The Pentagon, Washington, DC 20330 - Attn: Lt. Col. A.J. Chiota (1 copy)

HQ AFSC/SRLW, Andrews AFB, Washington, DC 20331 - Attn: Maj. J.M. Walton (1 copy)

HQ AFSC (DLCAM), Andrews AFB, Washington, DC 20331 - Attn: Maj. H. Axelrod (1 copy)

Air Force Weapons Laboratory, Kirtland AFB, NM 87117 - Attn: LR (1 copy)
AL (1 copy)

HQ Aeronautical Systems Div., Wright Patterson AFB, OH 45433 - Attn: XRF - Mr. Clifford Fawcett (1 copy)

Rome Air Development Command, Griffiss AFB, Rome, NY 13440 - Attn: Mr. R. Urtz (OCSE) (1 copy)

HQ Electronics Systems Div. (ESL), L.G. Hanscom Field, Bedford, MA 01730 - Attn: Mr. Alfred E. Anderson (XRT) (1 copy)
Technical Library (1 copy)

Air Force Rocket Propulsion Lab., Edwards AFB, CA 93523 - Attn: B.R. Bornhorst, (LKCG) (1 copy)

Air Force Aero Propulsion Lab., Wright Patterson AFB, OH 45433 - Attn: Col. Walter Moe (CC) (1 copy)

Dept. of the Air Force, Foreign Technology Division, Wright Patterson AFB, OH 45433 - Attn: PDTN (1 copy)

Commandant of the Marine Corps, Scientific Advisor (Code RD-1), Washington, DC 20380 (1 copy)

Aerospace Research Labs., (AP), Wright Patterson AFB, OH 45433 - Attn: Lt. Col. Max Duggins (1 copy)

Defense Intelligence Agency, Washington, DC 20301 - Attn: Mr. Seymour Berier (DTIB) (1 copy)

Central Intelligence Agency, Washington, DC 20505 - Attn: Mr. Julian C. Nall (1 copy)

Analytic Services, Inc., 5613 Leesburg Pike, Falls Church, VA 22041 - Attn: Dr. John Davis (1 copy)

Aerospace Corp., P.O. Box 92957, Los Angeles, CA 90009 - Attn: Dr. G.P. Millburn (1 copy)

Airesearch Manuf. Co., 9851-9951 Sepulveda Blvd., Los Angeles, CA 90009 - Attn: Mr. A. Colin Stancliffe (1 copy)

Atlantic Research Corp., Shirley Highway at Edsall Road, Alexandria, VA 22314 - Attn: Mr. Robert NalSmith (1 copy)

Avco Everett Research Lab., 2385 Revere Beach Parkway, Everett, MA 02149 - Attn: Dr. George Sutton (1 copy)
Dr. Jack Daugherty (1 copy)

Battelle Columbus Laboratories, 505 King Avenue, Columbus, OH 43201 - Attn: Mr. Fred Tietzel (STPIAC) (1 copy)

Bell Aerospace Co., Fubballo, NY 14240 - Attn: Dr. Wayne C. Solomon (1 copy)

Boeing Company, P.O. Box 3999, Seattle, WA 98124 - Attn: Mr. M.I. Gamble (2-, 460, MS 8C-88) (1 copy)

Electro-Optical Systems, 300 N. Halstead, Pasadena, CA 91107 - Attn: Dr. Andrew Jensen (1 copy)

General Electric Co., Space Division, P.O. Box 8555, Philadelphia, PA 19101 - Attn: Dr. R.R. Sigismondi (1 copy)

General Electric Co., 100 Plastics Avenue, Pittsfield, MA 01201 - Attn: Mr. D.G. Harrington (Rm. 1044) (1 copy)

General Research Corp., P.O. Box 3587, Santa Barbara, CA 93105 - Attn: Dr. R. Holbrook (1 copy)

DISTRIBUTION LIST (Continued)

Hercules, Inc., Industrial System Dept., Wilmington, DE 19899 - Attn: Dr. R.S. Voris (1 copy)

Hercules, Inc., P.O. Box 210, Cumberland, MD 21502 - Attn: Dr. Ralph R. Preckel (1 copy)

Hughes Research Labs., 3011 Malibu Canyon Road, Malibu, CA 90265 - Attn: Dr. D. Forster (1 copy)

Hughes Aircraft Co., Aerospace Group - Systems Division, Canoga Park, CA 91304 - Attn: Dr. Jack A. Alcalay (1 copy)

Hughes Aircraft Co., Centinela and Teale Streets, Bldg. 6, MS E-125, Culver City, CA 90230 - Attn: Dr. William Yates (1 copy)

Institute for Defense Analyses, 400 Army-Navy Drive, Arlington, VA 22202 - Attn: Dr. Alvin Schnitzler (1 copy)

Lawrence Livermore Laboratory, P.O. Box 808, Livermore, CA 94550 - Attn: Dr. R.E. Kidder (1 copy)
 Dr. E. Teller (1 copy)
 Dr. Joe Fleck (1 copy)

Los Alamos Scientific Laboratory, P.O. Box 1663, Los Alamos, NM 87544 - Attn: Dr. Keith Boyer (1 copy)

Lockheed Palo Alto Res. Lab., 3251 Hanover Street, Palo Alto, CA 94303 - Attn: L.R. Lunsford, Orgn. 52-24, Bldg. 201 (1 copy)

Mathematical Sciences Northwest, Inc., P.O. Box 1887, Bellevue, WA 98009 - Attn: Dr. Abraham Hertzberg (1 copy)

Massachusetts Institute of Technology, Lincoln Laboratory, P.O. Box 73, Lexington, MA 02173 - Attn: Dr. S. Edelberg (1 copy)
 Dr. L.C. Marquet (1 copy)

McDonnell Douglas Astronautics Co., 5301 Bolsa Avenue, Huntington Beach, CA 92647 - Attn: Mr. P.L. Klevatt,
 Dept. A3-830-BBFO, M/S 9 (1 copy)

McDonnell Douglas Research Labs., Dept. 220, Box 516, St. Louis, MO 63166 - Attn: Dr. D.P. Ames (1 copy)

North American Rockwell Corp., Autonetics Div., Anaheim, CA 92803 - Attn: Mr. T.T. Kumagi, C/476 Mail Code HA18 (1 copy)

Dr. Anthony N. Pirri, 30 Commerce Way, Woburn, MA 01801 (1 copy)

RAND Corp., 1700 Main Street, Santa Monica, CA 90406 - Attn: Dr. C.R. Culp/Mr. G.A. Carter (1 copy)

Raytheon Co., 28 Seyon Street, Waltham, MA 02154 - Attn: Dr. F.A. Horrigan (Res. Div.) (1 copy)

Raytheon Co., Boston Post Road, Sudbury, MA 01776 - Attn: Dr. C. Sonnenschien (Equip. Div.) (1 copy)

Raytheon Co., Bedford Labs, Missile Systems Div., Bedford, MA 01730 - Attn: Dr. H.A. Mehlhorn (1 copy)

Riverside Research Institute, 80 West End Street, New York, NY 10023 - Attn: Dr. L.H. O'Neill (1 copy)
 Dr. John Bose (1 copy)
 (HPEGL Library) (1 copy)

Rockwell International Corporation, Rocketdyne Division, Albuquerque District Office, 3636 Menaul Blvd., NE, Suite 211,
 Albuquerque, NM 87110 - Attn: C.K. Kraus, Mgr. (1 copy)

SANDIA Corp., P.O. Box 5800, Albuquerque, NM 87115 - Attn: Dr. Al Narath (1 copy)

Stanford Research Institute, Menlo Park, CA 94025 - Attn: Dr. F.T. Smith (1 copy)

Science Applications, Inc., 1911 N. Ft. Meyer Drive, Arlington, VA 22209 - Attn: L. Peckam (1 copy)

Science Applications, Inc., P.O. Box 328, Ann Arbor, MI 48103 - Attn: R.E. Meredith (1 copy)

Science Applications, Inc. 6 Preston Court, Bedford, MA 01703 - Attn: R. Greenberg (1 copy)

Science Applications, Inc. P.O. Box 2351, La Jolla, CA 92037 - Attn: Dr. John Asmus (1 copy)

Systems, Science and Software, P.O. Box 1620, La Jolla, CA 92037 - Attn: Alan F. Klein (1 copy)

Systems Consultants, Inc., 1050 31st Street, NW, Washington, DC 20007 - Attn: Dr. R.B. Keller (1 copy)

Thiokol Chemical Corp., WASATCH Division, P.O. Box 524, Brigham City, UT 84302 - Attn: Mr. J.E. Hansen (1 copy)

TRW Systems Group, One Space Park, Bldg. R-1, Rm. 1050, Redondo Beach, CA 90278 - Attn: Mr. Norman Campbell (1 copy)

United Technologies Research Center, 400 Main Street, East Hartford, CT 06108 - Attn: Mr. G.H. McLafferty (3 copies)

United Technologies Research Center, Pratt and Whitney Aircraft Div., Florida R&D Center, West Palm Beach, FL 33402 -
 Attn: Dr. R.A. Schmidtke (1 copy)
 Mr. Ed Pinsley (1 copy)

VARIAN Associates, EIMAC Division, 301 Industrial Way, San Carlos, CA 94070 - Attn: Mr. Jack Quinn (1 copy)

Vought Systems Division, LTV Aerospace Corp., P.O. Box 5907, Dallas, TX 75222 - Attn: Mr. F.G. Simpson, MS 254142 (1 copy)

Westinghouse Electric Corp., Defense and Space Center, Balt-Wash. International Airport - Box 746, Baltimore, MD 21203 -
 Attn: Mr. W.F. List (1 copy)

Westinghouse Research Labs., Beulah Road, Churchill Boro, Pittsburgh, PA 15235 - Attn: Dr. E.P. Riedel (1 copy)

DISTRIBUTION LIST (Continued)

United Technologies Research Center, East Hartford, CT 06108 - Attn: A.J. DeMaria (1 copy)
Airborne Instruments Laboratory, Walt Whitorian Road, Melville, NY 11746 - Attn: F. Pace (1 copy)
General Electric R&D Center, Schenectady, NY 12305 - Attn: Dr. Donald White (1 copy)
Cleveland State University, Cleveland, OH 44115 - Attn: Dean Jack Soules (1 copy)
EXXON Research and Engineering Co., P.O. Box 8, Linden, NJ 07036 - Attn: D. Grafstein (1 copy)
University of Maryland, Department of Physics and Astronomy, College Park, MD 20742 - Attn: D. Currie (1 copy)
Sylvania Electric Products, Inc., 100 Fergeson Drive, Mountain View, CA 94040 - Attn: L.M. Osterink (1 copy)
North American Rockwell Corp., Autonetics Divison, 3370 Miraloma Avenue, Anahelm, CA 92803 - Attn: R. Gudmundsen (1 copy)
Massachusetts Institute of Technology, 77 Massachusetts Avenue, Cambridge, MA 02138 - Attn: Prof. A. Javan (1 copy)
Lockheed Missile & Space Co., Palo Alto Research Laboratories, Palo Alto, CA 94304 - Attn: Dr. R.C. Ohlman (1 copy)
Polytechnic Institute of New York, Rt. 110, Farmingdale, NY 11735 - Attn: Dr. William T. Walter (1 copy)